Distributed actuation and control of a morphing tensegrity structure

Guanyu Lai [a], Andrew Plummer [a,*], David Cleaver [b]

[a] Centre for Power Transmission and Motion Control, Department of Mechanical Engineering, University of Bath, Bath, BA2 7AY, UK

[b] Department of Mechanical Engineering, University of Bath, Bath, BA2 7AY, UK

* Corresponding author.

E-mail addresses: guanyu.lai@hotmail.com (G. Lai), a.r.plummer@bath.ac.uk (A. Plummer), d.j.cleaver@bath.ac.uk (D. Cleaver).

Abstract

Structures and actuation systems need to be closely integrated together in the future to create faster, more efficient, lightweight dynamic machines. Such actuated structures would be used for morphing aircraft wings, lightweight actuated space structures, or in robotics. This approach requires actuators to be distributed through the structure. A tensegrity structure is a very promising candidate for this future integration due to its potentially excellent stiffness and strength-to-weight ratio, and the inherent advantage of being a multi-element structure into which actuators can be embedded. This paper presents methods for analysis of the structure geometry, for closed loop motion control, and includes experimental results for a structure actuated by lightweight pneumatic muscles. In a practical morphing tensegrity structure it cannot be assumed that tension and compression members always meet at a point. Thus a form-finding method has been developed to find stable geometries and determine stiffness properties for tensegrity structures with nodes of finite dimension. An antagonistic multi-axis control scheme has been developed for the shape position and motion control. In the experimental actuated tensegrity system presented the pneumatic muscles are controlled by on-off valves, for which a dead-band switching controller is designed based on a new stability criterion. The experimental system demonstrates accurate control of shape change while maintaining a desired level of internal pre-load in a stiff structure, showing considerable promise for future lightweight dynamic machines.

Keywords

Tensegrity

Form-finding

Multi-axis control

Pneumatic artificial muscle

Shape morphing

Variable geometry

1 Introduction

In the future, dynamic machines will require distributed actuation integrated with load-bearing structures, so that they are lighter, move faster, use less energy, and are more human-friendly. This integration has great potential to create smart structures that can provide better static and dynamic performance, redundancy and more adaptability than current designs.

An example application is in aerospace. Because of environmental and economic concerns, more efficient aircraft are required. A possible solution to improve efficiency is to allow an aircraft to adapt its aerodynamic shape for different flight regimes. Changing wing shape is not a new idea. Modern aircraft wings can change shape via actuated leading-edge slats, spoilers, ailerons, etc. A significant disadvantage of these devices is that they rely on the deflection of hinged, discrete control surfaces, which can, even under moderate levels of deflection, set up localised areas of severe adverse pressure gradient (typically along the hinge line) that produce regions of flow separation, and poor wing efficiency [1]. To reduce surface discontinuities and sharp edges, a possible solution is to replace part of the conventional wing with smart structures to perform distributed actuation, which allows subtle changes in curvature, thereby leading to better aerodynamic performance. Greater wing shape adaptability also allows better matching of the aerodynamic performance to the flight regime.

A truss structure can be used as the basis of a morphing structure by replacing some of the truss elements with linear actuators. The concept of variable geometry truss (VGT) structures was first proposed by Miura in 1984 [2] as a space deployable actuated structure, consisting of the repetition of an octahedral truss module in the longitudinal direction. Geometric transformations were achieved by changing the lengths of lateral members (telescopic beams). Based on the concept, Miura et al. developed a VGT robotic manipulator arm in 1985 that was the first shape morphing truss structure with three degrees of freedom [3]. The authors discussed other possible applications of the VGT structure, including support architectures for space stations and large actively controllable space structures.

In 2005, Ramrakhyani et al. developed a compliant cellular truss for wing morphing [4]. The structure used tendons as active members and a bending-type deformation was achieved by pulling and releasing appropriate tendons (cables). Later, Sofla et al., using tetrahedral truss unit cells, created a shape morphing hinged truss structure capable of bending, twisting and undulating [5]. The truss structure shape was changed by actuating shape memory wire actuators in an antagonistic manner. A novel spherical-pivotal joint, developed by Sofla et al. in 2007 [6], was used to connect several struts at a node. The joint could allow up to 18 struts to be connected at each node as though they met at a point. More recently, Moosavian et al. presented a novel design of underactuated parallel mechanism

for the application of morphing wingtip [7]. The structure of a conventional wingbox was replaced by active and passive linearly adjustable members. The mechanism could let the structure move in all six spatial degrees of freedom. Among the above VGT examples, the modular motion control has only been studied in detail by Moosavian. Other studies are intended to verify the feasibility of shape morphing without much consideration of external load, e.g. aerodynamic forces. Further studies would be valuable for creating structures with high stiffness and the desired motion capability under high loading conditions.

A tensegrity structure is a pin-jointed framework composed of struts and cables. The cable members are only able to exert tensile forces, while the struts are intended to be in compression when the structure is in static equilibrium. Note that struts are able to exert tensile loads and may do so in dynamic scenarios or with altered external loading. The cables, being tension members, can be lighter as they do not have to resist buckling. As its name suggests, the whole structure is required for 'integrity': it is stabilised by tensile member forces balancing compressive member forces, and the internal pre-load in the structure contributes a geometric component to the overall structure stiffness. All the members are axially loaded, which means there is no bending moment in any member or at any joint. A tensegrity structure is a promising basis for a morphing structure due to its potentially excellent stiffness and strength-to-weight ratio, and the inherent advantage of being a multi-element structure into which actuators can be embedded. The stiffness of many actuated systems is compromised by compliance (or even backlash) at joints when the load reverses direction; the pre-load within a tensegrity structure avoids this problem, unlike a VGT for example.

The first reported tensegrity structure was a sculpture built by Snelson in 1948 [8]. Fuller popularized the tensegrity concept, both in terms of man-made structures and a form commonly found in nature, and coined the term tensegrity as a contraction of "tensional integrity" [9]. Emmerich independently developed "self-tensioning structures" from the late 1950's [10]. As indicated in [8], the systematic study of tensegrity structure began in the 1970's, and attracted considerable interest from mathematicians from the 1980's.

Form-finding is the process of determining geometries and pre-stress distributions which give stable tensegrity structures. This has been widely studied, and researchers have developed analytical methods, e.g. [11-13], and numerical methods, e.g. [14-16]. Analytical methods have been used for tensegrities with relatively simple configuration and those that have a high level of symmetry. For more complicated and general tensegrities, numerical methods are require. Approaches are categorised in [17] as either kinematical or statical. Kinematical approaches look for a consistent set of element lengths, typically by increasing strut lengths while fixing cable lengths, or by reducing cable lengths while fixing strut lengths. Statical approaches search for configurations in which forces at nodes are in equilibrium.

Although some methods will identify structure forms which are stable, this is not sufficient to identify practically useful structures. For instance, the structure should also have high strength- and stiffness-to-mass ratios. Skelton and Oliveira [18] presented useful methods for optimising strength-to-mass ratio under compressive and bending loads for simple two-dimensional tensegrity structures. As stated by Plummer and Lai [19], more engineering issues need to be considered. In particular, in reality each node, i.e. where members meet, cannot simply be a point in space as normally assumed. Even if the lines of action of members are arranged to intersect at the same point in one configuration, shape-changing will alter this. Nodes are bodies in themselves connected to members by spatially separated joints.

Tensegrity structures can be made active by replacing some members with actuators. These can be single-acting actuators, either contracting actuators to replace cables, or extending actuators to replace struts. An active tensegrity structure could potentially achieve both good stiffness-to-mass ratio and many degrees of motion freedom. The motion kinematics and control of actuated tensegrity structures have received less attention than form-finding in the research literature. The need to combine dynamics and control considerations with structural optimisation presents added complexity. Experimental studies are particularly lacking at present. In an early study, optimal control was applied to alter the vibrational response of simulated tensegrity structures in [20]. Aldrich, *et al.* [21] who proposed a control method for tendon-driven robotic systems based on tensegrity structures. Skelton and Oliveira [18] investigated the dynamics and presented a control strategy for three-dimensional tensegrity structures, but with limited experimental validation. A difficulty is that cables can only take tension and this is a type of control saturation that complicates control analysis. Other examples of controllable tensegrity structures are the flight simulator motion system concept proposed in [22], and the adjustment of pre-stress to control vibrational response reported in [23]. Controllable tensegrity structures are included in Sultan's review paper [8].

Static tensegrity structures have found a number of applications. Kurilpa Bridge is a multiple-mast, cable-stay structure based on tensegrity principles [24]. In mechanical engineering, tensegrity has been explored for space applications [25-27], e.g. for large, lightweight truss-type space structures to support antennae and instrumentation [28]. Applications of actuated tensegrity structures are much less common. NASA proposed an actuated tensegrity structure to provide locomotion for a planetary exploration rover by rolling over the ground as a result of its shape changes [27]. The concept of using tensegrity structures for wing morphing, mechanically actuated via cables running through the structure, is described in [29] and [30], but this is theoretical only.

A potential application example in robotics is human-friendly robots. Future robots must interact safely with humans, e.g. in assistive or medical applications. Conventional industrial manipulators are heavy, making it difficult for them to behave gently and safely, so a more responsive alternative with better force-mass ratio is required [31, 32]. Another viable application of actuated tensegrity structures is snake-arm robots. These robots are slender manipulators with many joints, designed to perform remote handling operations in confined and hazardous environments [33]. They can squeeze through small openings and crawl around obstacles. The nuclear industry has been driving the development of these manipulators because of the needs of working in radiation and confined spaces [34, 35].

This paper concerns the design and control of multi-axis actuated tensegrity structures. A form-finding method is developed in Section 2 which can be used to determine if a proposed structure is stable in a range of shapes. The method considers nodes of finite dimension, i.e. members do not need to meet at a point. A multi-axis control scheme for a structure with antagonistic actuation is described in Section 3. Pneumatic muscles supplied by on-off valves are proposed as an example actuation technology, and a switching dead band controller is presented to realise both motion and pre-load control. The stability of the dead band controller is studied using the describing function technique. Section 4 presents the setup of an experimental actuated tensegrity system. Experimental results and discussion are contained in Section 5. Finally, conclusions are drawn in Section 6.

2 Geometry and stability of tensegrity structures

2.1 Finding equilibrium node positions

A form-finding method for structures in which members all meet at a point at each node has been described in [19]. A variety of other form finding methods have been proposed using the same assumption [11-16]. A practical shape-changing structure cannot be constructed in which several struts and cables are pin-jointed at exactly the same point in space. A physically realisable arrangement is to have nodes of finite size and connect members to nodes via joints that are spatially separated. An example is given in Fig. 1. The members are connected together by nodes of finite size. The circles indicate pin (i.e. spherical) joints and the bodies of the nodes are not shown. A node with finite dimensions has an additional 3 degrees of freedom in rotation. Thus it is necessary to take into account the node torsional stiffness dependent on member stiffnesses and forces. In this section, a form-finding method for this case of nodes with finite dimensions is derived. The method includes the orientation of nodes in the calculation of member lengths and considers not only the resultant force of member forces on each node but also their resultant moment. The node material is assumed to be rigid, and the members (struts and cables) are assumed to exhibit linear stiffness, i.e. they obey Hooke's Law. A block diagram

for finding the equilibrium configuration of a tensegrity structure is presented in Fig. 2. The novelty of this approach is the inclusion of nodes of finite dimension.

Consider a pin jointed structure such as that shown in Fig. 1. There are *n* nodes (in this case 6) and *m* structural members (in this case 13). All the members are axially loaded. There is no bending moment in any member or torque at any joint. Typically, each member is designed to support either a compressive load (in which case it is called a strut), or a tensile load (in which case it is called a cable). Cables are depicted with red thinner lines. The structure is normally pre-loaded. This is usually necessary when the structure is supporting an external load so that the forces in the cables and struts

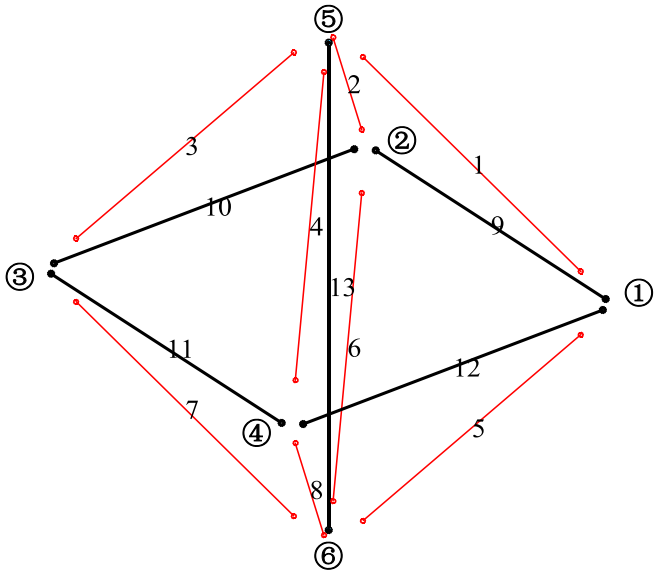

Fig. 1. Example of structure with nodes of finite size

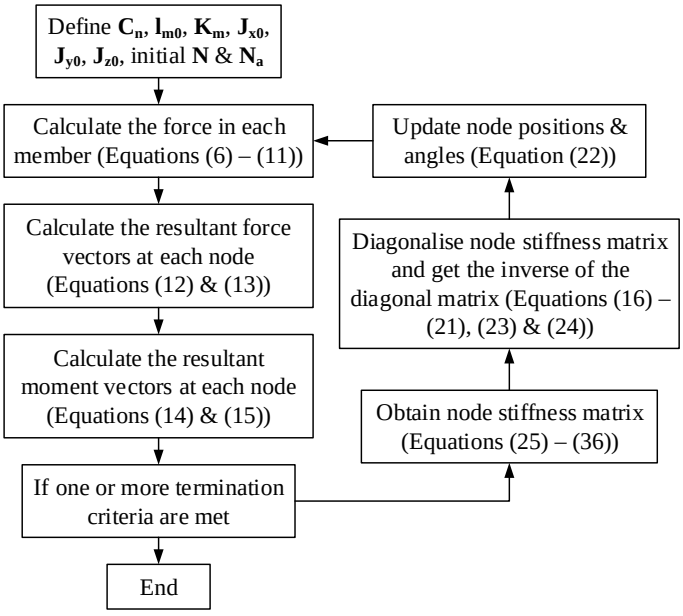

Fig. 2 Process for finding the equilibrium configuration of tensegrity structures with finite nodes

remain in the right direction (tension or compression), and may be required to give a statically stable structure via its resulting geometric stiffness even with no external load (see [36] for a detailed analysis of tensegrity stability). In the following, the stiffness of each member is specified, and the form-finding method is used to iteratively move the node positions and orientations until the resultant force and moment at each node are zero to within a chosen tolerance. The resulting node positions and orientations are those when the structure is in static equilibrium, a condition which may not exist. The method can be used to find the structural equilibrium state with or without external loads applied to nodes in the structure.

The connectivity matrix, $\mathbf{C_n} \in \Re^{m\times n}$, defines the configuration of the structure. Each row in the matrix $\mathbf{C_n}$ corresponds to a member of the structure and contains a −1 and a +1 entry indicating the two nodes that the member spans, and otherwise the elements are zero. Taking the structure of Fig. 1 as an example, the first four rows are:

$$\mathbf{C_n} = \begin{bmatrix} -1 & 0 & 0 & 0 & 1 & 0 \\ 0 & -1 & 0 & 0 & 1 & 0 \\ 0 & 0 & -1 & 0 & 1 & 0 \\ 0 & 0 & 0 & -1 & 1 & 0 \\ \vdots & \vdots & \vdots & \vdots & \vdots & \vdots \end{bmatrix} \tag{1}$$

Let $\mathbf{N} \in \Re^{3\times n}$ be a matrix of node coordinates and $\mathbf{N_a} \in \Re^{3\times n}$ be a matrix of node angles:

$$\mathbf{N} = \begin{bmatrix} \mathbf{x} \\ \mathbf{y} \\ \mathbf{z} \end{bmatrix}; \quad \mathbf{N_a} = \begin{bmatrix} \boldsymbol{\varphi} \\ \boldsymbol{\theta} \\ \boldsymbol{\psi} \end{bmatrix} \tag{2}$$

where $\mathbf{x} = [x_1 \quad x_2 \quad \cdots \quad x_n]$, $\mathbf{y} = [y_1 \quad y_2 \quad \cdots \quad y_n]$ and $\mathbf{z} = [z_1 \quad z_2 \quad \cdots \quad z_n]$ are the node linear positions; the three orthogonal rotations are roll $\boldsymbol{\varphi} = [\varphi_1 \quad \varphi_2 \quad \cdots \quad \varphi_n]$, pitch $\boldsymbol{\theta} = [\theta_1 \quad \theta_2 \quad \cdots \quad \theta_n]$ and yaw $\boldsymbol{\psi} = [\psi_1 \quad \psi_2 \quad \cdots \quad \psi_n]$ about the *x*-, *y*- and *z*-axes, respectively.

Consider $\mathbf{J_{x0}} \in \Re^{m\times n}$, $\mathbf{J_{y0}} \in \Re^{m\times n}$ and $\mathbf{J_{z0}} \in \Re^{m\times n}$ as matrices that in turn give the joint spatial positions in the *x*-, *y*- and *z*-axes relative to node centres when there is no node rotation. When the nodes rotate, the spatial positions of a joint on node *k* and with member *i* attached can be related by:

$$\begin{bmatrix} \mathbf{J_x}(i,k) \\ \mathbf{J_y}(i,k) \\ \mathbf{J_z}(i,k) \end{bmatrix} = \mathbf{R_z}(\psi_k)\mathbf{R_y}(\theta_k)\mathbf{R_x}(\varphi_k) \begin{bmatrix} \mathbf{J_{x0}}(i,k) \\ \mathbf{J_{y0}}(i,k) \\ \mathbf{J_{z0}}(i,k) \end{bmatrix} \tag{3}$$

where $\mathbf{J_x} \in \Re^{m\times n}$, $\mathbf{J_y} \in \Re^{m\times n}$ and $\mathbf{J_z} \in \Re^{m\times n}$ are matrices of joint positions in the *x*-, *y*- and *z*-axes relative to node centres when the nodes have rotated,

$$\mathbf{J_x} = \begin{bmatrix} \mathbf{J}_{\mathbf{x}1} \\ \mathbf{J}_{\mathbf{x}2} \\ \vdots \\ \mathbf{J}_{\mathbf{x}m} \end{bmatrix}; \quad \mathbf{J_y} = \begin{bmatrix} \mathbf{J}_{\mathbf{y}1} \\ \mathbf{J}_{\mathbf{y}2} \\ \vdots \\ \mathbf{J}_{\mathbf{y}m} \end{bmatrix}; \quad \mathbf{J_z} = \begin{bmatrix} \mathbf{J}_{\mathbf{z}1} \\ \mathbf{J}_{\mathbf{z}2} \\ \vdots \\ \mathbf{J}_{\mathbf{z}m} \end{bmatrix} \tag{4}$$

and $\mathbf{R_x}(\theta)$, $\mathbf{R_y}(\theta)$ and $\mathbf{R_z}(\theta)$ are rotation matrices that rotate vectors by an angle θ about the *x*-, *y*- and *z*-axes and are given by [37]:

$$\mathbf{R_x}(\theta) = \begin{bmatrix} 1 & 0 & 0 \\ 0 & \cos\theta & -\sin\theta \\ 0 & \sin\theta & \cos\theta \end{bmatrix}; \quad \mathbf{R_y}(\theta) = \begin{bmatrix} \cos\theta & 0 & \sin\theta \\ 0 & 1 & 0 \\ -\sin\theta & 0 & \cos\theta \end{bmatrix}; \quad \mathbf{R_z}(\theta) = \begin{bmatrix} \cos\theta & -\sin\theta & 0 \\ \sin\theta & \cos\theta & 0 \\ 0 & 0 & 1 \end{bmatrix} \tag{5}$$

In Eq. (3), *i* and *k* refer to the row (member) and column (node) index of the matrix respectively.

Each member is represented by a vector from its '−1' node to its '+1' node. Member vectors and member lengths need to be calculated including the orientation of the nodes as well as the deviations of the members from the node centres. The matrix of member vectors $\mathbf{\tilde{M}} \in \Re^{3\times m}$ can be derived in two steps, by first calculating vectors between node centres:

$$\mathbf{M} = \mathbf{N}\mathbf{C_n}^{\mathrm{T}} \tag{6}$$

with columns as indicated by:

$$\mathbf{M} = \begin{bmatrix} \mathbf{m}_1 & \mathbf{m}_2 & \cdots & \mathbf{m}_m \end{bmatrix} \tag{7}$$

and then including the effect of joint offset and node orientation on member *i* as follows:

$$\tilde{\mathbf{M}} = \sum_{i=1}^{m} (\mathbf{m}_i + \begin{bmatrix} \mathbf{J}_{\mathbf{x}i} \\ \mathbf{J}_{\mathbf{y}i} \\ \mathbf{J}_{\mathbf{z}i} \end{bmatrix} \mathbf{C_n}^{\mathrm{T}} \mathbf{S_1}_i^{\mathrm{T}}) \mathbf{S_1}_i \tag{8}$$

where $\mathbf{S_1}_i \in \Re^{1\times m}$ is a single-entry vector with the i^{th} entry being 1 and the rest of the entries being 0. A vector $\mathbf{l_m} \in \Re^{m\times 1}$ of member lengths can be calculated from $\mathbf{\tilde{M}}$ and each element in $\mathbf{l_m}$ is:

$$l_{mi} = \sqrt{\tilde{\mathbf{m}}_i^{\mathrm{T}} \tilde{\mathbf{m}}_i} \tag{9}$$

where

$$\tilde{\mathbf{m}}_i = \begin{bmatrix} \tilde{\mathbf{M}}(1,i) & \tilde{\mathbf{M}}(2,i) & \tilde{\mathbf{M}}(3,i) \end{bmatrix}^{\mathrm{T}} \tag{10}$$

i.e. $\tilde{\mathbf{m}}_i$ is a column in $\mathbf{\tilde{M}}$.

Let the vector of free (unloaded) member lengths be $\mathbf{l_{m0}}$, so the force in each member is given by:

$$\mathbf{f_m} = \mathbf{K_m}(\mathbf{l_m} - \mathbf{l_{m0}}) \tag{11}$$

where $\mathbf{K_m} \in \Re^{m\times m}$ is a diagonal matrix of the member stiffnesses. Projecting these forces along the member vectors contained in $\mathbf{\tilde{M}}$ gives the matrix of member force vectors $\mathbf{F_m} \in \Re^{3\times m}$:

$$\mathbf{F_m} = \tilde{\mathbf{M}}\mathrm{diag}(\begin{bmatrix} f_{m1}/l_{m1} & \cdots & f_{mi}/l_{mi} & \cdots & f_{mm}/l_{mm} \end{bmatrix}) \tag{12}$$

where diag() is a diagonal matrix with its vector argument providing the sequence of main diagonal elements, and f_{mi} is the i^{th} entry in $\mathbf{f_m}$. Force vectors of positive magnitude in $\mathbf{F_m}$ point from the '−1' to the '+1' nodes defined in $\mathbf{C_n}$. The matrix $\mathbf{F_n} \in \Re^{3\times n}$ of resultant force vectors at each node is given by:

$$\mathbf{F_n} = -\mathbf{F_m}\mathbf{C_n} + \mathbf{F_e} \tag{13}$$

where $\mathbf{F_e} \in \Re^{3\times n}$ is a matrix of external force vectors at each node. For a structure with no externally applied load, $\mathbf{F_e}$ is a matrix with all its entries being zero.

The member forces are combined to give not only a resultant force on each node (Eq. (13)) but also a resultant moment. The two matrices $\mathbf{F_m}$ and $\mathbf{F_n}$ are written as:

$$\mathbf{F_m} = \begin{bmatrix} \mathbf{F_{mx}} \\ \mathbf{F_{my}} \\ \mathbf{F_{mz}} \end{bmatrix}; \quad \mathbf{F_n} = \begin{bmatrix} \mathbf{F_{nx}} \\ \mathbf{F_{ny}} \\ \mathbf{F_{nz}} \end{bmatrix} \tag{14}$$

The matrix $\mathbf{M_n} \in \Re^{3\times n}$ of resultant moment vectors at each node can be calculated as follows:

$$\mathbf{M_n} = \begin{bmatrix} \mathbf{F_{my}}(\mathbf{C_n} \circ \mathbf{J_z}) - \mathbf{F_{mz}}(\mathbf{C_n} \circ \mathbf{J_y}) \\ \mathbf{F_{mz}}(\mathbf{C_n} \circ \mathbf{J_x}) - \mathbf{F_{mx}}(\mathbf{C_n} \circ \mathbf{J_z}) \\ \mathbf{F_{mx}}(\mathbf{C_n} \circ \mathbf{J_y}) - \mathbf{F_{my}}(\mathbf{C_n} \circ \mathbf{J_x}) \end{bmatrix} \tag{15}$$

where $\circ$ is the Hadmard product (entrywise product) giving a matrix which is the element by element product of two matrices with the same dimensions, and

$$\mathbf{M_n} = \begin{bmatrix} \mathbf{M_{nx}} \\ \mathbf{M_{ny}} \\ \mathbf{M_{nz}} \end{bmatrix} \tag{16}$$

$\mathbf{K_n} \in \Re^{6n\times 6n}$ is a node stiffness matrix which relates node displacements and rotations in each Cartesian direction to the corresponding change in node forces and moments. By expressing the node linear and angular position coordinates in a column vector $\mathbf{n_v} \in \Re^{6n\times 1}$ and the node force and moment vectors in a similar manner in $\mathbf{f_v} \in \Re^{6n\times 1}$,

$$\begin{aligned} \mathbf{n_v} &= \begin{bmatrix} \mathbf{x} & \mathbf{y} & \mathbf{z} & \boldsymbol{\varphi} & \boldsymbol{\theta} & \boldsymbol{\psi} \end{bmatrix}^{\mathrm{T}} \\ \mathbf{f_v} &= \begin{bmatrix} \mathbf{F_{nx}} & \mathbf{F_{ny}} & \mathbf{F_{nz}} & \mathbf{M_{nx}} & \mathbf{M_{ny}} & \mathbf{M_{nz}} \end{bmatrix}^{\mathrm{T}} \end{aligned} \tag{17}$$

small changes in these two column vectors can be related by $\mathbf{K_n}$ as follows:

$$\Delta\mathbf{f_v} = \mathbf{K_n}\Delta\mathbf{n_v} \tag{18}$$

The calculation of $\mathbf{K_n}$ is discussed in Section 2.2.

The stiffness matrix $\mathbf{K_n}$ can be transformed into a diagonal matrix $\boldsymbol{\Omega} \in \Re^{6n\times 6n}$ through a similarity transformation. To achieve this, a linear transformation is applied to $\mathbf{n_v}$ and $\mathbf{f_v}$ using a matrix $\mathbf{P_b} \in \Re^{6n\times 6n}$

whose columns are the vectors of a new basis. The two vectors can be transformed to the new basis by left-multiplying their elements by the inverse of $\mathbf{P_b}$:

$$\Delta\mathbf{n_w} = \mathbf{P_b}^{-1}\Delta\mathbf{n_v}; \quad \Delta\mathbf{f_w} = \mathbf{P_b}^{-1}\Delta\mathbf{f_v} \tag{19}$$

This gives:

$$\Delta\mathbf{f_w} = \mathbf{P_b}^{-1}\mathbf{K_n}\mathbf{P_b}\Delta\mathbf{n_w} \tag{20}$$

If the columns of $\mathbf{P_b}$ are the eigenvectors of $\mathbf{K_n}$, the diagonalization of $\mathbf{K_n}$ is achieved. Hence,

$$\Delta\mathbf{f_w} = \mathbf{\Omega}\Delta\mathbf{n_w} \tag{21}$$

and the diagonal matrix $\mathbf{\Omega}$ has the eigenvalues of $\mathbf{K_n}$ along its diagonal.

The form-finding method is an iterative method that starts from an initial estimation of node positions and orientations, and repeatedly updates them until the resultant force and moment at each node are zero to within a chosen tolerance. The change in node position and orientation at each iteration is to move the nodes to positions and orientations where the resultant forces and moments are zero according to the latest stiffness matrix. However, this also causes a change in the stiffness matrix, so iterations are required. The updated node positions and orientations are given by:

$$\mathbf{n_w}(i+1) = \mathbf{n_w}(i) - \mathbf{\Omega'}(i)\mathbf{f_w}(i) \tag{22}$$

where $\mathbf{\Omega'} \in \Re^{6n\times 6n}$ is a modified inverse of $\mathbf{\Omega}$, with the six rigid body modes being removed and replaced with zeros. The inverse is derived by first sorting the elements on the diagonal of $\mathbf{\Omega}$:

$$\mathbf{\Omega} = \mathrm{diag}(\begin{bmatrix}\lambda_1 & \lambda_2 & \cdots & \lambda_{3n}\end{bmatrix}) \tag{23}$$

where $|\lambda_k|>|\lambda_{k+1}|$, and the associated columns in $\mathbf{P_b}$ accordingly. Then,

$$\mathbf{\Omega'} = \mathrm{diag}(\begin{bmatrix}1/\lambda_1 & \cdots & 1/\lambda_{3n-6} & 0 & \cdots & 0\end{bmatrix}) \tag{24}$$

The six rigid modes that this inverse removes are not relevant to altering the internal forces on the nodes. This is because in these modes, all the nodes translate or rotate together, and there is no relative motion between the nodes.

For a specific implementation of the form-finding method, Eq. (22) can be combined with one or more termination criteria, e.g. the root mean square value of the resultant forces at all nodes is zero to within a chosen tolerance.

2.2 Calculating the stiffness matrix

When moving a single node in any direction, not only the member forces in the members attached to the single node will be changed but also the resultant force acting on that node and all nodes to which it is connected will be changed. These changes can be attributed to both the change in magnitude of the member forces and their change in direction. The extent of these changes is dependent upon the node stiffness. The node stiffness (also known as tangent stiffness) can be considered as composed of two

parts, one of which is the elastic stiffness that depends on the axial stiffness of the members, and the other is the geometric stiffness that depends on the size of member forces and their orientation.

The calculation of the node stiffness matrix $\mathbf{K_n}$ is based on the method described in [38] and is extended by including the orientation of nodes. The node material itself is assumed to be rigid. $\mathbf{J} \in \Re^{3n\times m}$ is a Jacobian matrix that describes the rate of change of member lengths with respect to node positions and is arranged as follows:

$$\mathbf{J} = \begin{bmatrix} \mathbf{C_n}^{\mathrm{T}}\mathrm{diag}(\mathbf{C_n}\mathbf{x}^{\mathrm{T}})\mathrm{diag}(\begin{bmatrix}1/l_{m1} & \cdots & 1/l_{mm}\end{bmatrix}) \\ \mathbf{C_n}^{\mathrm{T}}\mathrm{diag}(\mathbf{C_n}\mathbf{y}^{\mathrm{T}})\mathrm{diag}(\begin{bmatrix}1/l_{m1} & \cdots & 1/l_{mm}\end{bmatrix}) \\ \mathbf{C_n}^{\mathrm{T}}\mathrm{diag}(\mathbf{C_n}\mathbf{z}^{\mathrm{T}})\mathrm{diag}(\begin{bmatrix}1/l_{m1} & \cdots & 1/l_{mm}\end{bmatrix}) \end{bmatrix} \tag{25}$$

remembering that l_{mi} is the length of member i. The product of the two diagonal matrices in each term of Eq. (25) gives the components of the unit vectors of the members in that axis. When rotating a single node, it will also produce a series of changes that are similar to those when moving a node. The effect of node rotation can be considered by resolving the rotational movement into an equivalent translational movement of the joints. $\mathbf{J_r} \in \Re^{3n\times m}$ is a Jacobian matrix that relates the rate of change of member lengths to the node angles, and is given by:

$$\mathbf{J_r} = \sum_{i=1}^{m} \mathbf{R_{l}}_i{}^{\mathrm{T}}\mathbf{J}\mathbf{S_3}_i \tag{26}$$

where $\mathbf{S_3}_i \in \Re^{m\times m}$ is a single-entry matrix whose entry in the i^{th} row and i^{th} column is 1, and $\mathbf{R_l}_i \in \Re^{3n\times 3n}$ is a matrix for member i that converts the rotational movement of nodes into the equivalent translational movement of joints and is given by:

$$\mathbf{R_l}_i = \begin{bmatrix} 0_{n,n} & \mathrm{diag}(\mathbf{J_z}_i) & -\mathrm{diag}(\mathbf{J_y}_i) \\ -\mathrm{diag}(\mathbf{J_z}_i) & 0_{n,n} & \mathrm{diag}(\mathbf{J_x}_i) \\ \mathrm{diag}(\mathbf{J_y}_i) & -\mathrm{diag}(\mathbf{J_x}_i) & 0_{n,n} \end{bmatrix} \tag{27}$$

where $0_{n,n} \in \Re^{n\times n}$ is a zero matrix. Including the effect of node rotation, the elastic stiffness $\mathbf{K_e} \in \Re^{6n\times 6n}$ for the complete structure is given by:

$$\mathbf{K_e} = \begin{bmatrix} \mathbf{J} \\ \mathbf{J_r} \end{bmatrix} \mathrm{diag}(\begin{bmatrix} g_1 & \cdots & g_m \end{bmatrix}) \begin{bmatrix} \mathbf{J} \\ \mathbf{J_r} \end{bmatrix}^{\mathrm{T}} \tag{28}$$

where g_i is the axial stiffness of member i.

$\mathbf{q} \in \Re^{m\times 1}$ is a vector of member tension coefficients (sometimes called force densities) and is defined as:

$$\mathbf{q} = \begin{bmatrix} f_{m1}/l_{m1} & \cdots & f_{mi}/l_{mi} & \cdots & f_{mm}/l_{mm} \end{bmatrix}^{\mathrm{T}} \tag{29}$$

The matrices $\mathbf{C_n}$ and $\mathbf{J}$ and the vector $\mathbf{q}$ are written as:

$$\mathbf{C_n} = \begin{bmatrix} \mathbf{C_{n1}} \\ \mathbf{C_{n2}} \\ \vdots \\ \mathbf{C_{nm}} \end{bmatrix}; \quad \mathbf{J} = \begin{bmatrix} \mathbf{J}_1 & \mathbf{J}_2 & \cdots & \mathbf{J}_m \end{bmatrix}; \quad \mathbf{q} = \begin{bmatrix} q_1 \\ q_2 \\ \vdots \\ q_m \end{bmatrix} \tag{30}$$

The geometric stiffness $\mathbf{K_g} \in \Re^{6n\times 6n}$ is a block partitioned matrix, written as:

$$\mathbf{K_g} = \begin{bmatrix} \mathbf{K_{g11}} & \mathbf{K_{g12}} \\ \mathbf{K_{g21}} & \mathbf{K_{g22}} \end{bmatrix} \tag{31}$$

The block $\mathbf{K_{g11}} \in \Re^{3n\times 3n}$ gives the relationship between the linear node displacements and the resultant node forces, and is [38]:

$$\mathbf{K_{g11}} = \mathbf{I_3} \otimes (\mathbf{C_n}^{\mathrm{T}} \mathrm{diag}(\mathbf{q}) \mathbf{C_n}) - \mathbf{J} \mathrm{diag}(\mathbf{q}) \mathbf{J}^{\mathrm{T}} \tag{32}$$

where $\mathbf{I_3} \in \Re^{3\times 3}$ is an identity matrix and $\otimes$ is the Kronecker product (direct matrix product) that forms a block matrix by reproducing $\mathbf{C_n}^{\mathrm{T}}\mathrm{diag}(\mathbf{q})\mathbf{C_n}$ three times along the diagonal. The block $\mathbf{K_{g12}} \in \Re^{3n\times 3n}$ relates the node forces to the angular node displacements, given by:

$$\mathbf{K_{g12}} = \sum_{i=1}^{m} (\mathbf{I_3} \otimes (\mathbf{C_{n}}_i{}^{\mathrm{T}} q_i \mathbf{C_{n}}_i) - \mathbf{J}_i q_i \mathbf{J}_i{}^{\mathrm{T}}) \mathbf{R_l}_i \tag{33}$$

The block $\mathbf{K_{g21}} \in \Re^{3n\times 3n}$ determines the node moments produced by linear node displacements, given by:

$$\mathbf{K_{g21}} = \mathbf{K_{g12}}^{\mathrm{T}} \tag{34}$$

Finally, the block $\mathbf{K_{g22}} \in \Re^{3n\times 3n}$ determines the node moments given by angular node displacements, and can be found from:

$$\mathbf{K_{g22}} = \sum_{i=1}^{m} \mathbf{R_l}_i{}^{\mathrm{T}} (\mathbf{I_3} \otimes (\mathbf{C_{n}}_i{}^{\mathrm{T}} q_i \mathbf{C_{n}}_i) - \mathbf{J}_i q_i \mathbf{J}_i{}^{\mathrm{T}}) \mathbf{R_l}_i \tag{35}$$

The node stiffness can be derived by adding the elastic and the geometric stiffnesses given by the two Eqs. (28) and (31) together:

$$\mathbf{K_n} = \mathbf{K_e} + \mathbf{K_g} \tag{36}$$

Thus the stiffness matrix which includes the node rotational degrees of freedom as well as the (conventional) translational co-ordinates is derived.

2.3 Kinematics of an example actuated tensegrity structure

2.3.1 Configuration of the example structure

The geometrical configuration of an example actuated tensegrity structure is depicted in Fig. 3. The example structure has 13 struts (members 1 to 13 in thick lines) and 20 cables (thinner lines), and can be considered as three connected 'unit cells' of the same configuration. The members are jointed to 12 nodes of finite size. The circles indicate pin joints, and the bodies of the nodes are not shown. Assuming that four tensile members (cables) in the centre part of the structure are actuated (members 15, 18, 21 and 24), it is possible to produce three independent motions by controlling these members antagonistically, whilst also controlling the internal force of the structure. This structure was first presented in [19].

In preparation for the use of the example structure in this research, statically stable instances of the structure with different actuator lengths are determined using the algorithm developed in Section 2.1. Some of its physical properties are listed in **Table 1**. Note that the joints are positioned at the specified offsets away from the node centre in the direction of the corresponding member when the structure is in its neutral position.

Table 1. Physical properties of the example tensegrity structure

Initial strut length in $\mathbf{l_{m0}}$	0.2284 m
Initial cable length in $\mathbf{l_{m0}}$	0.1786 m
Strut stiffnesses g_1 to g_{13} in the diagonal of $\mathbf{K_m}$ based on 6 mm diameter carbon fibre solid rod with Young's modulus of 181 GPa	2.3262×10^7 N/m
Cable stiffnesses g_{14} to g_{33} in the diagonal of $\mathbf{K_m}$ based on 1 mm diameter steel wire with Young's modulus of 200 GPa	8.7947×10^5 N/m
Offset of strut joint from node centre in $\mathbf{J_{x0}}$, $\mathbf{J_{y0}}$ and $\mathbf{J_{z0}}$	0.005 m
Offset of cable joint from node centre in $\mathbf{J_{x0}}$, $\mathbf{J_{y0}}$ and $\mathbf{J_{z0}}$	0.008 m

2.3.2 Actuation of example tensegrity structure

It is shown in this section that the example tensegrity structure can change between stable positions when the four embedded actuators change length. Initial results have been introduced in [19, 39]. Figs. 3 and 4 show the structure when the actuators are at their neutral (mid) position, and their lengths are the same as the equivalent cables in the other unit cells. The force levels are illustrated in Fig. 3 in the equilibrium state with no external forces. Orthogonal views of the same structure are shown in Fig. 4. By altering the relevant initial (unloaded) member lengths to emulate realistic actuator displacements, the method of Section 2.1 can be used to find an equilibrium state in which the member forces are in the right direction, i.e. the struts are all in compression and the cables are all in tension, and are at a

realistic force level. The same process can be performed in the case where an external load is applied, which is presented in [40].

Fig. 5 illustrates a set of actuation examples. The top view in Fig. 5 shows the structural equilibrium state when the initial lengths of members 15 and 18 are contracted by 14.8% and members 21 and 24 are extended by 20.2%. This causes the structure to bend in the *xy*-plane (compare with top view in Fig. 4). The front view in Fig. 5 is an example of shear motion in the *yz*-plane, achieved by contracting members 15 and 24 by 21.5 % and extending members 18 and 21 by 17.5%. The third motion (side view in Fig. 5) approximates to a twist about the *y*-axis and is caused by the contraction of members 15 and 21 (21.5%) and the extension of members 18 and 24 (17.9%). By adjusting the relative contraction and extension of the actuated members, the structure pre-load can be changed. A practical way of doing this is through closed loop force control, as shown in later sections.

In this structure, the offsets of the joints from the node centres have been chosen to give static stability for the range of actuated shapes shown. Although not proven here, it may be appreciated that, with the joints offset from each node centre in the direction of the members, tensile members provide the node with positive geometric angular stiffness, whereas compressive members provide negative geometric angular stiffness which will encourage instability (effectively buckling). Thus the effect of the tensile members must be dominant compared to the compressive members to stabilise a node in rotation. If the cable joint offsets in Table 1 were progressively reduced the angular node stiffnesses would reduce until such point as the structure becomes unstable. This has been established empirically, but an analytical method for determining this threshold has not been determined. Thus the joint offsets have been determined by trial and error, bearing in mind practical constraints given the intention to build a real structure.

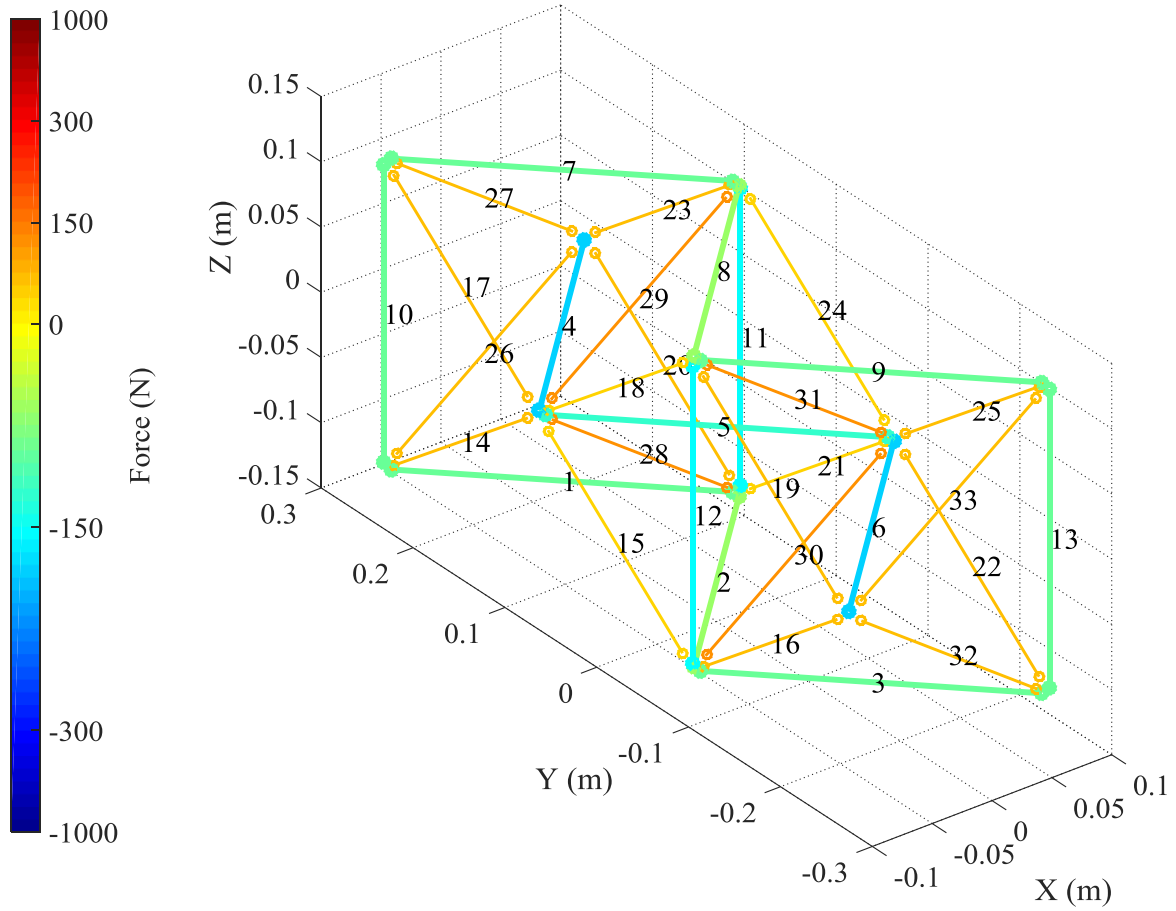

Fig. 3. Geometrical configuration of the example actuated tensegrity structure with finite node dimensions when unactuated, isometric view

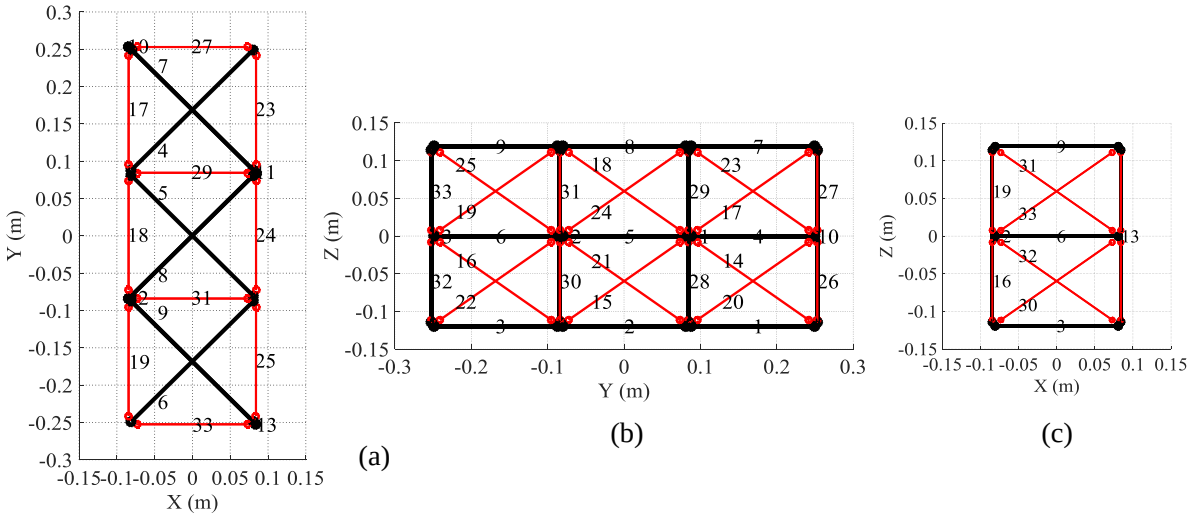

Fig. 4. Example structure when unactuated: **(a)** Top view, **(b)** Front view and **(c)** Side view

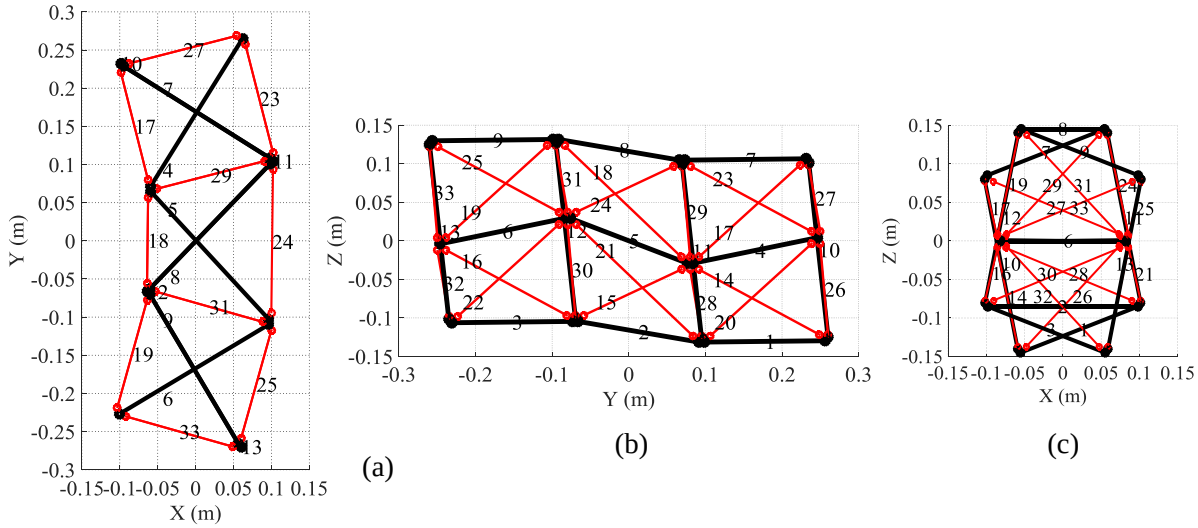

Fig. 5. Actuation examples: **(a)** Bend mode in top view, **(b)** Shear mode in front view and **(c)** Twist mode in side view

3 Antagonistic multi-axis control scheme

3.1 Overview

The example actuated tensegrity structure needs to be controlled to realise the three degrees of freedom (bend, shear and twist) and to maintain an appropriate level of pre-load in the course of deformation. A multi-axis control scheme is proposed to achieve simultaneous motion and force control. This example structure is used to illustrate the approach, but the same method could be applied to other tensegrity structures in which a collection of members are replaced by actuators in such a way as to allow shape change. Either cables or struts, or a mixture, could be replaced by actuators, but replacing cables gives the advantage that the actuators only need to create tension and so buckling is not a concern. Any actuator only needs to act uni-directionally. The maximum number of positional degrees of freedom will always be at least one less than the number of actuators due to the need for independent pre-load control.

Pneumatic artificial muscles supplied by on-off solenoid valves are adopted for the experimental system to be described in Section 4. Pneumatic muscles are single-acting (contracting) actuators with excellent force-to-weight ratio which make them highly suitable for this application. On-off solenoid valves are very cost-effective control valves, but need to be sufficiently fast acting to achieve adequate control accuracy. The hardware is described in detail in Section 4. A control scheme is designed which is appropriate for this type of actuation, in particular using bang-bang control due to the use of on-off valves.

The multi-axis control scheme is shown in Fig. 6. It is developed according to a general co-ordinate transformation framework for multi-axis motion control [41] and the overall concept was proposed in [19]. It is based on a modal decomposition to provide both independent displacement degrees of freedom, and independent pre-load (or internal force) control loops. This control scheme can be applied to any number of actuators, from two and above. Actuators are divided into different combinations to achieve multiple degrees of freedom. There are d position loops and $a–d$ force loops in the multi-axis control scheme, where d is the number of independent degrees of freedom and a is the number of actuators.

For the position control, the position demands are defined as the deviation of the structure in d degrees of freedom from the nominal neutral position and are represented by a vector $\boldsymbol{\delta}_\mathbf{r} \in \Re^{d\times 1}$. The actuator displacements away from their own zero positions, e.g. mid stroke, are measured giving a vector $\boldsymbol{\delta}_\mathbf{a} \in \Re^{a\times 1}$. For the force control, it is assumed that the actuator forces are measured, which gives a vector $\mathbf{f}_\mathbf{a} \in \Re^{a\times 1}$. The measured forces need to be transformed into one or more independently controllable internal force variables which are the elements in vector $\mathbf{f}_\mathbf{d} \in \Re^{(a-d)\times 1}$, for which the demand vector is $\mathbf{f}_\mathbf{r} \in \Re^{(a-d)\times 1}$.

The actuator displacements $\boldsymbol{\delta}_\mathbf{a}$ need to be transformed to virtual feedbacks $\boldsymbol{\delta}_\mathbf{c} \in \Re^{d\times 1}$ which define the shapes that are to be independently controlled (workspace position co-ordinates to use robotics terminology). This is achieved by a transformation $\mathbf{P}$. $\mathbf{P}$ and the other signal transformations in Fig. 6 could be based on full kinematic models, or they could be constant linear matrix transformations if displacements are small. The latter is used here. Then, $\mathbf{P} \in \Re^{d\times a}$, $\mathbf{C} \in \Re^{a\times d}$, $\mathbf{D} \in \Re^{a\times(a-d)}$, and $\mathbf{Q} \in \Re^{(a-d)\times a}$. The compensators in the position and force loops might be proportional-integral or other types of controller, and would often be implemented in workspace co-ordinates [41]. In this paper, bang-bang control is used with a dead band, and it is appropriate to implement the switching function in actuator space (labelled as 'Compensator' in Fig. 6). The output of each actuator position compensator is determined by the error between the demand and the feedback positions transformed to actuator space, and is:

$$G = \begin{cases} 1 & \text{if error} > B \\ 0 & \text{if } -B \le \text{error} \le B \\ -1 & \text{if error} < -B \end{cases} \tag{37}$$

where B is the level of position tolerance. The dead band compensator G_f for the force loop is defined in the same way, but with a tolerance of B_f.

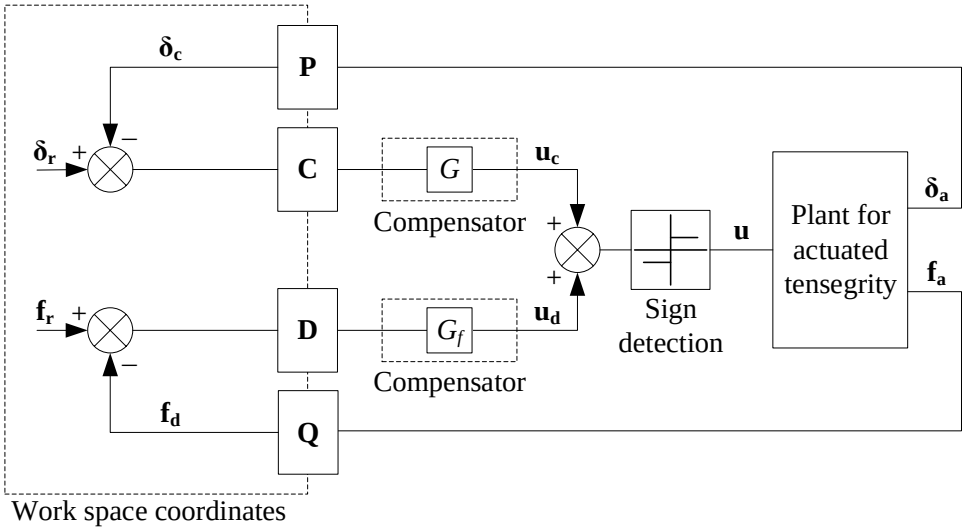

Fig. 6. Multi-axis control scheme for an actuated tensegrity structure

3.2 Control for the example structure

For the example actuated tensegrity structure, $a = 4$ and $d = 3$, as there are three degrees of freedom (bend, shear and twist) to be implemented by embedding four actuators into the structure. So for this application the vector of actuator displacements $\boldsymbol{\delta}_\mathbf{a}$ is:

$$\boldsymbol{\delta}_\mathbf{a} = \begin{bmatrix} s_1 \\ s_2 \\ s_3 \\ s_4 \end{bmatrix} \tag{38}$$

where s_i is the measured displacement from the neutral position of actuator i.

The matrix $\mathbf{P}$ defines the workspace position coordinates, i.e.:

$$\boldsymbol{\delta}_\mathbf{c} = \mathbf{P}\boldsymbol{\delta}_\mathbf{a} \tag{39}$$

The choice of $\mathbf{P}$ depends on user requirements, and is a set of actuator position differences in this work. The four actuators are of the same length when the tensegrity structure is unactuated at its neutral position. The actuators are divided into three different combinations and are controlled by considering the deviation from the neutral position, which gives:

$$\begin{aligned} (s_1 + s_2) - (s_3 + s_4) &= 2\alpha \\ (s_1 + s_3) - (s_2 + s_4) &= 2\beta \\ (s_2 + s_3) - (s_1 + s_4) &= 2\gamma \end{aligned} \tag{40}$$

where α, β and γ are the actuator position differences defining bend, shear and twist respectively. Thus, the position demand, $\boldsymbol{\delta}_\mathbf{r}$, is a column vector containing 3 elements. Each element represents a demanded actuator position difference for that specific degree of freedom (bend, shear or twist). And from Eq. (40) the position transformation matrix is:

$$\mathbf{P} = \frac{1}{2} \times \begin{bmatrix} 1 & 1 & -1 & -1 \\ 1 & -1 & 1 & -1 \\ -1 & 1 & 1 & -1 \end{bmatrix} \tag{41}$$

As proved in [41], the matrix **C** which transforms the position loop control signal components back to actuator co-ordinate space must conform to $\mathbf{PC} = \mathbf{I_3}$, where $\mathbf{I_3} \in \Re^{3\times 3}$ is the identity matrix. The following choice conforms to this requirement:

$$\mathbf{C} = \mathbf{P}^{\mathrm{T}} \tag{42}$$

Also from [41], to provide internal force control in co-ordinates which are consistent with the workspace position control variables, it is necessary that $\mathbf{PD} = \mathbf{0}$, i.e. the columns of **D** are the vectors which form the basis of the null space of matrix **P**. In this case there is only one force control loop, and **D** is chosen as follows:

$$\mathbf{D} = \begin{bmatrix} 1 & 1 & 1 & 1 \end{bmatrix}^{\mathrm{T}} \tag{43}$$

Likewise, for transformation **Q** from actuator forces to internal 'workspace' force $\mathbf{f_d}$, it is required that $\mathbf{PQ}^{\mathrm{T}} = \mathbf{0}$ [41]. The following choice is made,

$$\mathbf{Q} = \frac{1}{4} \times \begin{bmatrix} 1 & 1 & 1 & 1 \end{bmatrix} \tag{44}$$

which gives $\mathbf{f_d}$ as the average force of the four actuators. Although this choice of transformations has been presented for the example structure of Section 2.3, the method adopted can be applied generally.

The multi-axis control scheme for the example structure has a set of three position loops and a force loop, creating two control signal vectors which are transformed back into actuator space, and then each element passed through the dead band switching function of Eq. (37). The resulting vectors $\mathbf{u_c}$ and $\mathbf{u_d}$ are added together. The combined vector contains 4 elements and passes through a sign detection block, yielding +1 for a positive element or −1 when the element is negative, and zero otherwise. This forms a signal vector **u** for the control of the valve set. Each actuator is controlled by two on-off valves. The high pressure supply valve is opened if the corresponding element in the signal vector **u** is +1. The discharge valve is opened if the element is −1. Otherwise, both valves are closed to maintain a fixed amount (mass) of air in the actuator.

3.3 Stability analysis for dead band controller

The stability analysis has been presented in [42]. For completeness, it is summarised here. The stability of the system is related to the nonlinearity of the dead band controller. A simplified model, analogous to the position control of the antagonistic actuators, is used in the stability analysis and is shown in Fig. 7. A damper and a spring are placed in parallel with a mass attached at one end and a

movable base at the other end. The dead band controller can control the base to move left or right at a constant speed v to reach different position demands for y. The input speed is equivalent to the actuator motion when a valve opens, the spring k_s and the damping c_s represent the damped stiffness of the actuators, and the mass m_s represents the inertia driven by them. Although this is a highly simplified model, it allows us to establish an analytical stability criterion which provides insight as to how key parameters effect the dynamic stability of the controlled structure.

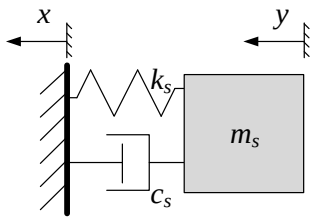

Fig. 7. Simplified system analogous to the position control of an antagonist group of actuators

The simplified system can be used to study the stability of position control. y_d is the position demand signal. The dead band controller G of Eq. (37) is used. With only the position loop in this control system, the sign detection block is not required. The product of G and v gives the input velocity $\dot{x}$ to the plant. Applying Newton's Second Law, the mathematical model of the simplified system is:

$$m_s\ddot{y} = k_s(x-y) + c_s(\dot{x}-\dot{y}) \tag{45}$$

And the arrangement of the control system is illustrated in block diagram form in Fig. 8.

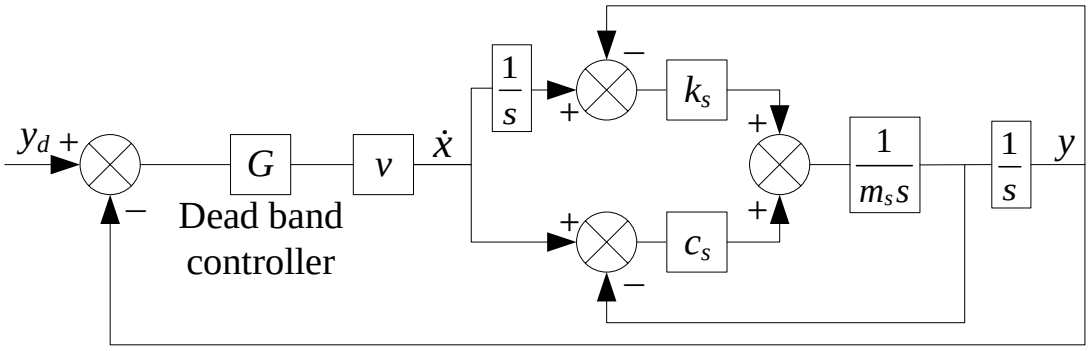

Fig. 8. Control of the simplified system

To analyse the control system, the describing function technique is used [43]. The technique approximates the non-linear part, i.e. the dead band controller, by considering the fundamental component of a Fourier series. The describing function is defined as:

$$G_N(M) = \frac{a_1}{M} \tag{46}$$

where a_1 is the amplitude of the fundamental component in the Fourier series and M is the amplitude of the excitation waveform.

To simplify the Fourier transform, the excitation and the non-linear output are assumed to be even. So sine terms in the Fourier series can be eliminated. The integrand has a quarter wave symmetry which implies not only does the wave of the integrand have half wave symmetry but each of its half waves is also symmetrical about its mid-point [43]. Consequently, the integration range is reduced to one quarter of the period. And the fundamental component can be calculated by quadrupling the result.

$$a_1 = 4 \cdot \frac{2}{T_s}\left[\int_0^{t_2} G\cos(\omega t)dt + \int_{t_2}^{T_s/4} G\cos(\omega t)dt\right]$$
$$a_1 = \frac{4}{\pi}\sin(\omega t_2) \tag{47}$$

where T_S is the period, t_2 is the transition time from G = 1 to 0, ω is the frequency and t is the time variable. At the transition time t_2, the value of the excitation waveform is equal to the tolerance B which gives:

$$B = M\cos(\omega t_2) \tag{48}$$

By combining Eqs. (46) to (48), the describing function of the dead band controller for position is derived and for $M > B$:

$$G_N(M) = \frac{4}{\pi M}\sqrt{1-\left(\frac{B}{M}\right)^2} \tag{49}$$

Otherwise, if $M \le B$, $G_N(M) = 0$. From Eq. (49) it has a maximum value of

$$G_N(M)_{\max} = \frac{2}{\pi B} \tag{50}$$

The stability of the non-linear control system can be examined on a Nyquist plot of the product of the describing function and the linear part of the open loop transfer function. However, as the describing function is a function of amplitude and the linear part is a function of frequency, it is more convenient to conduct the examination by plotting the frequency response of the linear part and the negative reciprocal of the describing function. There is a chance of limit cycle behaviour if they intersect [43]. From Fig. 8, the linear part of the open loop transfer function of the simplified system in the frequency domain is:

$$D(j\omega) = \frac{k_s + j\omega c_s}{j\omega(k_s - m_s\omega^2 + j\omega c_s)} \tag{51}$$

Therefore, for guaranteed stability of the control system, there should be no intersection. This requires:

$$D(j\omega_{lc}) > -\frac{1}{vG_N(M)_{\max}} \tag{52}$$

where ω_{lc} is the frequency at which the phase of $D(j\omega)$ is −180°.

Eq. (51) can be decomposed into the product of an integrator and an expression $A(j\omega)$ which is:

$$A(j\omega) = \frac{k_s + j\omega c_s}{(k_s - m_s\omega^2) + j\omega c_s} \tag{53}$$

The frequency at which $\angle A(j\omega) = -90°$ can be found from the right-angle triangle formed by numerator and denominator complex numbers plotted on a phasor diagram, giving ω_{lc} as:

$$\omega_{lc} = \sqrt{\frac{{k_s}^2}{m_s k_s - {c_s}^2}} \tag{54}$$

By using Eqs. (50) to (52) and (54), the requirement for stability is given by:

$$\frac{m_s k_s - {c_s}^2}{c_s k_s} < \frac{\pi B}{2v} \tag{55}$$

This analytical solution indicates that increasing the mass can make the system unstable and increasing the position tolerance helps to stabilise the system. It also indicates that the control system is more likely to be stable with higher damping. The criterion for guaranteed stable response is used as a general rule to achieve stable control of the tensegrity prototype in the experimental study described in Section 5 and the simulation study presented in [44].

4 Experimental system

4.1 System description

An experimental actuated tensegrity system has been constructed to verify the design and control methods proposed. The experimental system has three constituents which are the pneumatic actuation system, the tensegrity structure and the control system, shown schematically in Fig. 9. The structure in the experimental system replicates two unit cells of the same geometry as the example tensegrity structure in Section 2. Thus the experimental structure has 9 compressive members and 14 tensile members. Among the tensile members, four are pneumatic actuators embedded in the bottom unit cell. The actuators are pneumatic artificial muscles (PAMs) each controlled by two on-off solenoid valves. The supply pressure is kept at 6 bar gauge pressure during the experiment. Short lengths of polyurethane tubing with 4 mm internal diameter are used for the connection of the pneumatic hardware. An xPC system is used for real-time control and data acquisition (DAQ). The xPC system has a host PC for the user interface, and a target environment (a target PC and an interface module) running controller code in real-time.

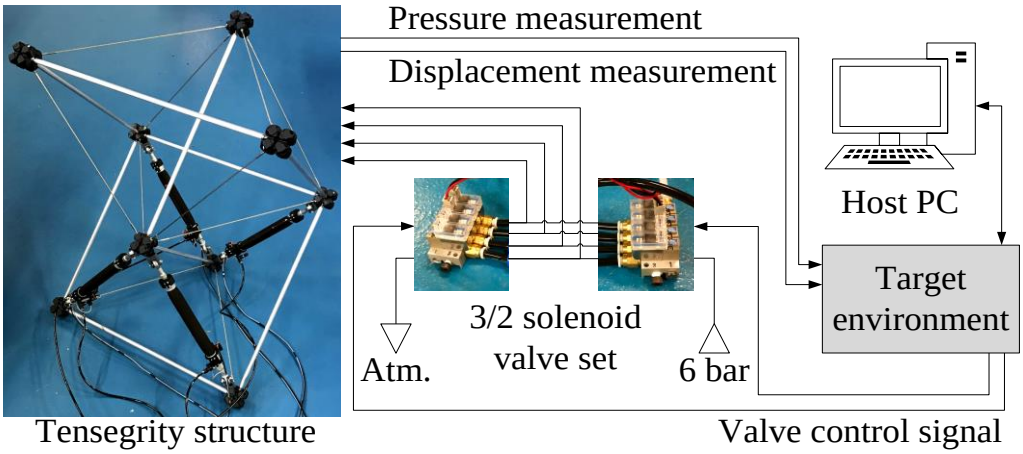

Fig. 9. Schematic diagram of the experimental actuated tensegrity system

4.2 Pneumatic system

The connection of one PAM is shown diagrammatically in Fig. 10. Each PAM is controlled by two 3/2 on-off solenoid valves. One solenoid valve is connected to a 6 bar gauge pressure supply and is used to pressurise the PAM. The other solenoid valve is connected to atmosphere for the discharge of the PAM. When both valves are off (i.e. shut), the compressed air is trapped in the PAM, thereby maintaining the position if the force does not change. A pressure transducer (type SPTE-P10R-S6-V-2.5K from Festo) is connected at the PAM inlet to measure the pressure within the muscle. A draw-wire sensor (type WPS-250-MK30-P10 from Micro-Epsilon) with a resolution of 0.1 mm is used for the displacement measurement. A specially designed mounting is used to hold the displacement sensor at one end of the PAM with the wire pulled out and attached at the other end. The sensor assembly CAD drawing and photos are shown in Fig. 11.

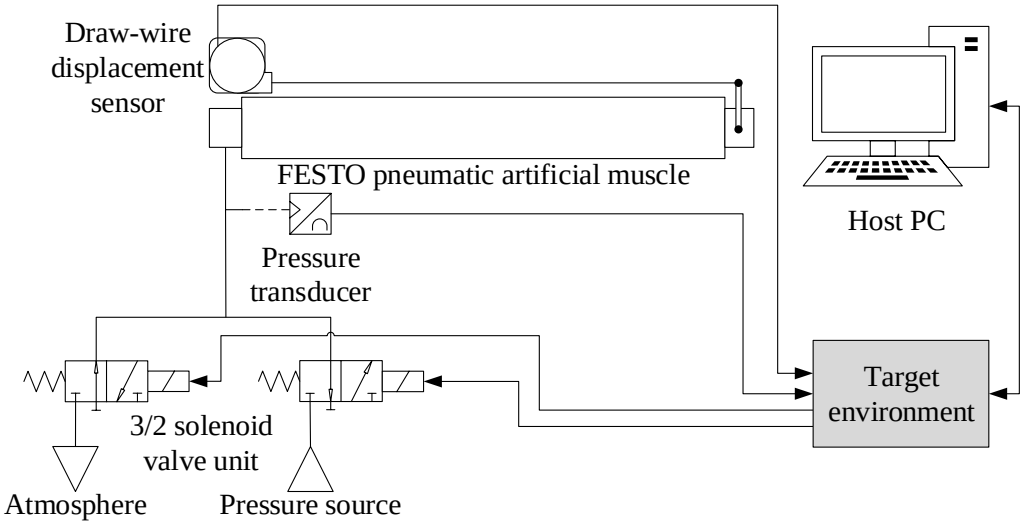

Fig. 10. Schematic diagram for the connection of one PAM

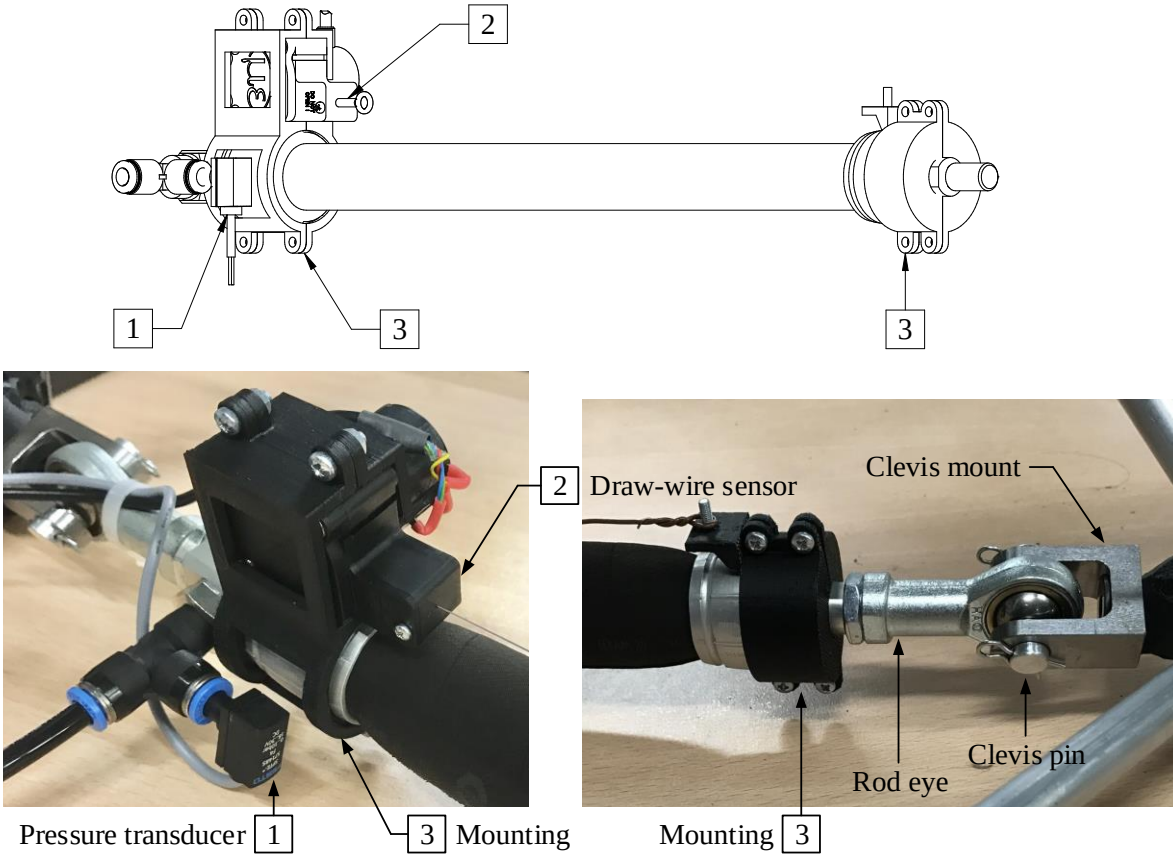

Fig. 11. Sensor assembly CAD drawing and close-up photos

The PAMs in this research are type DMSP-20-290N-RM-CM produced by Festo. They have several advantages over conventional cylinder-type pneumatic actuators, e.g. they are frictionless and have a high force to weight ratio [45]. The muscle is constructed by wrapping a pressure-tight rubber tube with inextensible high strength fibres. The fibres made of aramid yarns are orientated to create a rhomboidal pattern and are layered to build a three-dimensional grid structure. When air flows into the PAM, the rubber tube expands in its circumferential direction, which generates a pulling force and a contraction movement in the longitudinal direction. The chosen PAM has an internal diameter of 20 mm and a nominal length of 290 mm, when the muscle is unpressurised. The maximum contraction of the PAM is 25% of its nominal length and its operational range is between 0 and 6 bar gauge pressure.

As shown in Fig. 11, a rod eye (type SGS-M10×1.25 also from Festo) with spherical bearing is screwed on the male thread at each end of the PAM and attached to a clevis mount, which in turn is screwed to the node. The clevis linkage allows a certain amount of misalignment of the attached part permitting a restricted rotation of the PAM in three dimensions.

The valve set comprises eight 3/2 on-off solenoid valves and two 4 station manifold bases. The valves are high speed switching valves from SMC with response time of no more than 10 ms. Among them, four are type V114A-5LU and the other four are type V124A-5LU. The valves of the same type

are mounted on the same manifold base. The two manifold bases are of the same type (VV100-S41-04-M5 from SMC). The compressed air is supplied to the PAMs via port 1 on the manifold base for the V114A valves and discharged to the atmosphere also through port 1 on the manifold base for the V124A valves. The inlet of the PAM is connected to port 2 on both manifold bases using a T connector. For both manifold bases, channels to port 3 are blocked by epoxy resin plugs so that the air is trapped within the PAM when both valves are off (zero voltage).

4.3 Tensegrity structure

The experimental tensegrity structure has two unit cells with a total of 23 members, and its unit cell configuration is equivalent to the example structure presented in Section 2. The nine compressive members with ball studs screwed into their ends are struts made of aluminium alloy tubes, having an outside diameter of 12.7 mm and a wall thickness of 3.18 mm. In addition to the four PAMs, the remaining tensile members are 3 mm stainless steel cables. There is a left hand swage stud and a right hand swage stud at each end of the stainless steel cable, which means the effective cable length can easily be adjusted. The 23 members are connected together through nine nodes 3D printed in ABS.

The structure is sized according to the mid-stroke position of the PAM, i.e. the length when the PAM contracts by 12.5%. So the range of motion is ± 12.5% from the mid-stroke position of the PAM. At the neutral position, the distances from one centre of the node to the other for each compressive member and tensile member are 654.4 mm and 566.8 mm, respectively. Due to the finite size of the node, the length of either the compressive member or the tensile member is shorter than the corresponding distance between node centres. It is 614.4 mm (from one centre of the ball stud to the other) for compressive member and is 524.8 mm (from one end to the other) for tensile member.

4.4 Control system

The xPC system for the control of the experimental actuated tensegrity system allows a controller to be developed as a Simulink model and the model parameters to be tuned on the host PC while running the model in real-time on the target environment. The system provides real-time monitoring of the pressure within each PAM, the displacement of each PAM, and both the position and force demands and the corresponding feedbacks calculated from the measured signals. It is possible to estimate the tensile force exerted by the PAM from measurements of pressure and displacement using an analytical model. However this has not been found to be sufficiently accurate in practice [40]. Instead, a 2D lookup table is used to determine the force based on the pressure and displacement measurements. Fig. 12 is a graphic representation of the data in the lookup table. The data are derived by testing the PAM on an Instron machine at different pressures.

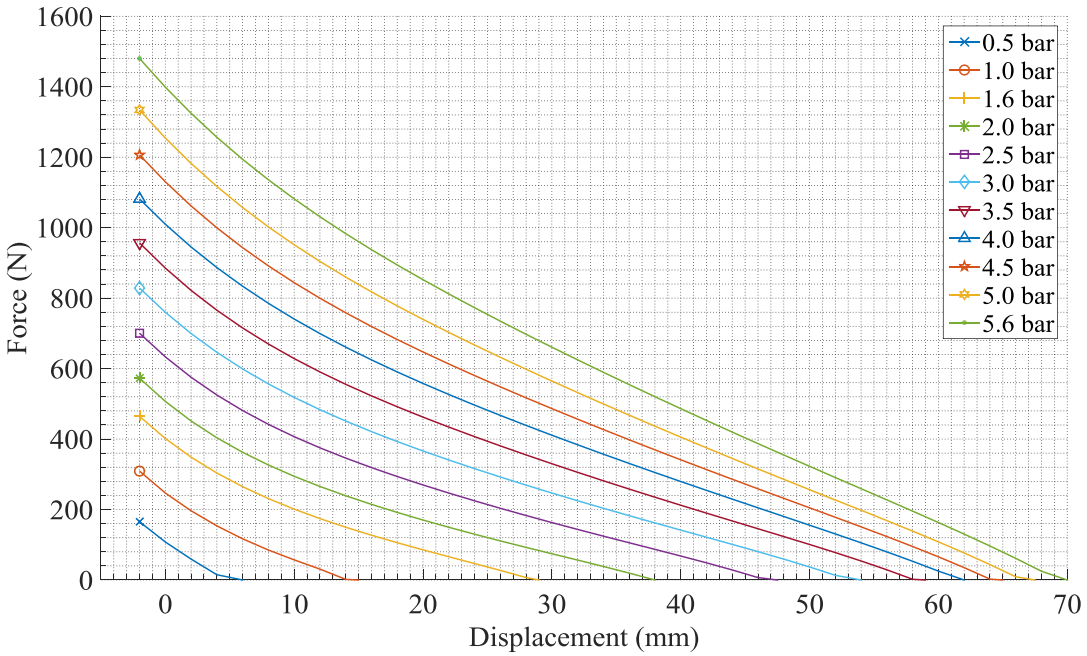

Fig. 12. Graphic representation of the data in the 2D lookup table

The target PC is fitted with a high-speed multifunction DAQ board from National Instruments, type NI PCI-6251. Eight analogue input channels are used to read voltages from the four pressure transducers (1 V/bar) and the four draw-wire sensors (0.04 V/mm). Eight digital channels I/O are used to control the on-off valves. There is a power supply unit, a valve drive board, and a shielded I/O connector block (type NI SCB-68 from National Instruments) in the interface module. The digital signals are connected to transistors to drive the valves with 24 V signals. The shielded I/O connector block is connected to the DAQ board using a cable (type NI SHC68-68-EPM) from National Instruments.

More details of the experimental system can be found in Lai's PhD thesis [40].

5 Experimental results

5.1 Small amplitude square wave position demand

The multi-axis control scheme of Section 3 has been tested using the experimental system described in Section 4. For all the tests, the tensegrity structure is initially in the neutral position and the sample time is fixed at 10 ms. In the first series of tests, a square wave of 10 mm amplitude and 3 s period is used for each degree of freedom in turn, with a constant pre-load force demand of 200 N.

Firstly, the tolerance settings are $B = 0.2$ mm and $B_f = 3$ N to see the performance of the experimental actuated tensegrity system under a tight position tolerance. The experimental results in bend, shear and twist are shown in Figs. 13 to 15. It can be seen that the system oscillates intermittently in the three degrees of freedom. For the motion in shear and twist, the oscillations only occur in one direction of the motion. This is probably due to both the intrinsic asymmetry of the mass distribution in the tensegrity structure and the imperfect assembly of the structure.

According to the stability criterion described in Section 3, a wider dead band tolerance can help to stabilise the system. The force tolerance B_f is kept the same as the system acts in compliance with the force demand. The position tolerance B is increased to 0.4 mm. The results are demonstrated in Figs. 16 to 18. The experimental tensegrity system achieves stable responses across all the three degrees of freedom. Steady-state errors in the position control are acceptable and the pre-load is well kept to be close to 200 N during the motion.

The third set of tests in this section uses different force demands, keeping the same tolerance settings in the previous set. The results are compared in Figs. 19 to 21. It can be seen that when the force demand is small, the system responds faster. This is probably due to the air compressibility, as more air is required to flow into the muscle when the pre-load is higher. Another possible reason is that, with a small force demand, the friction at the joints is less.

To see the influence of change in mass, the experimental system is tested by removing the unactuated top unit cell. The position tolerance is reduced again to 0.2 mm for these tests. The results are shown in Figs. 22 to 24. With less inertia to be driven, the system is able to respond well with the tight position tolerance. This is consistent with the stability criterion (Eq. (55)) which shows that the system with a dead band controller is more likely to be stable with lower mass.

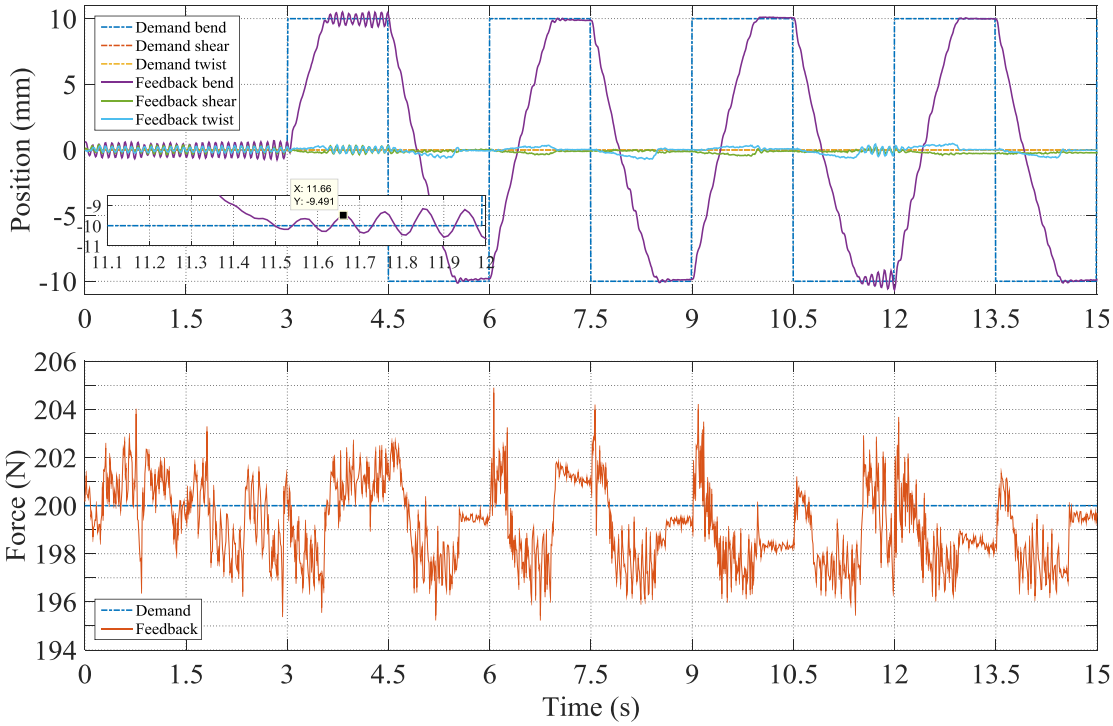

Fig. 13. Experimental responses with square position demand of 10 mm in bend, force demand of 200 N, B = 0.2 mm and B_f = 3 N

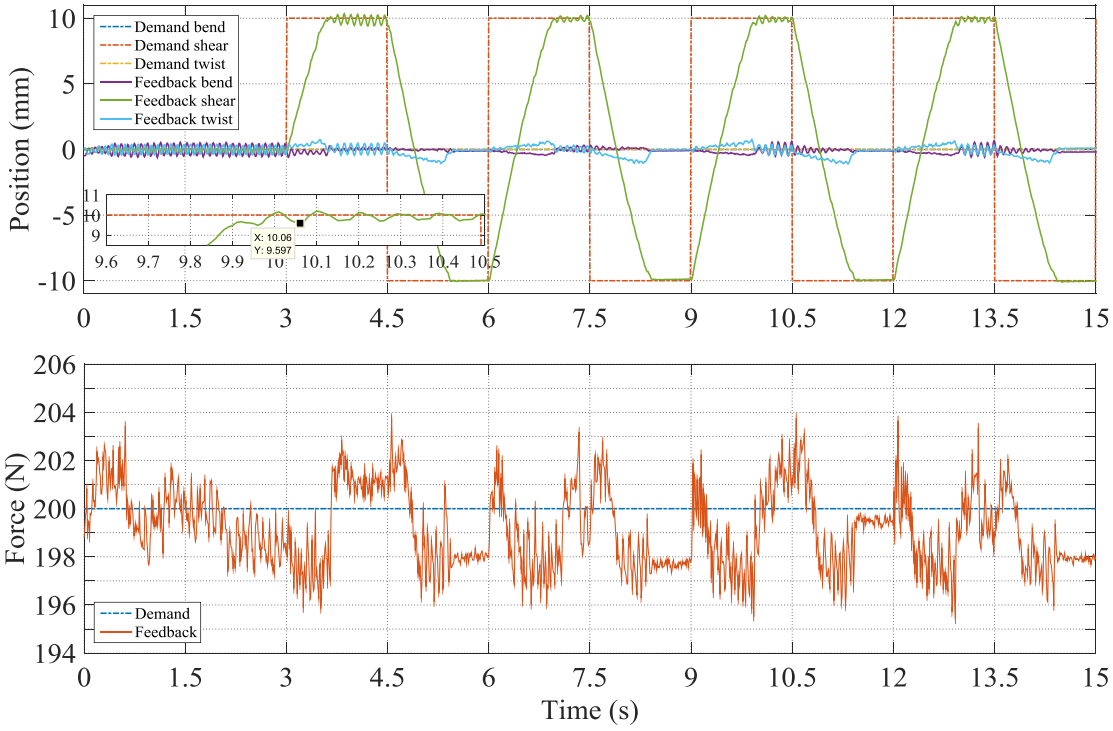

Fig. 14. Experimental responses with square position demand of 10 mm in shear, force demand of 200 N, B = 0.2 mm and B_f = 3 N

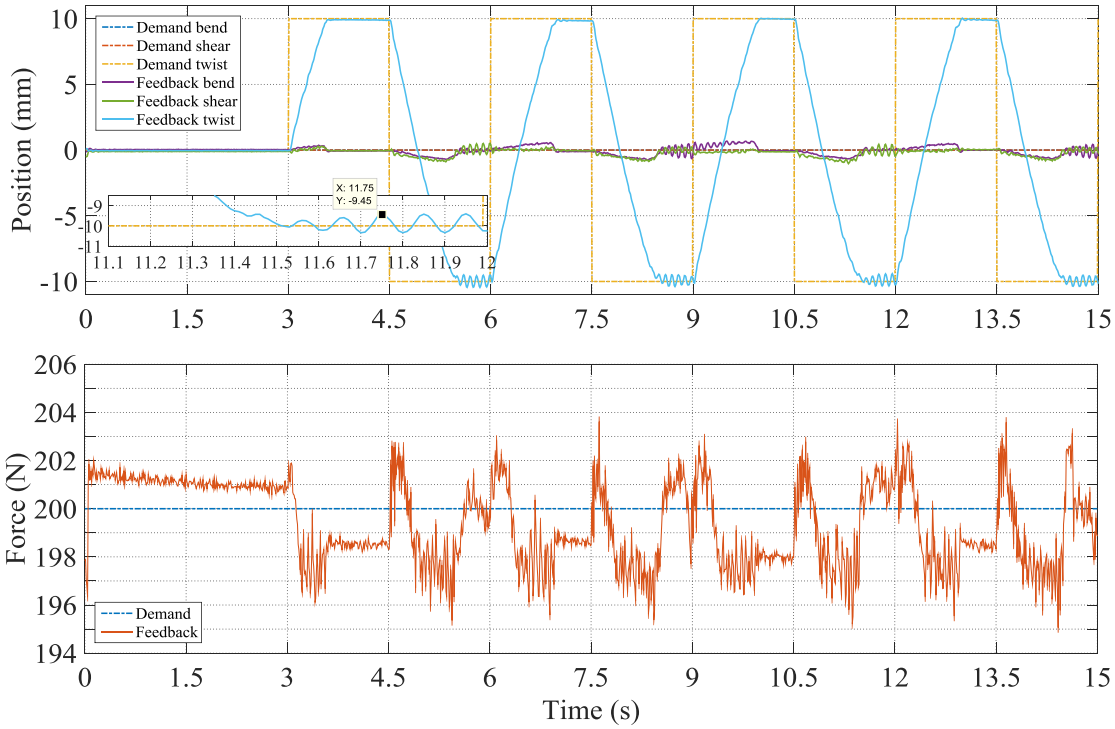

Fig. 15. Experimental responses with square position demand of 10 mm in twist, force demand of 200 N, B = 0.2 mm and B_f = 3 N

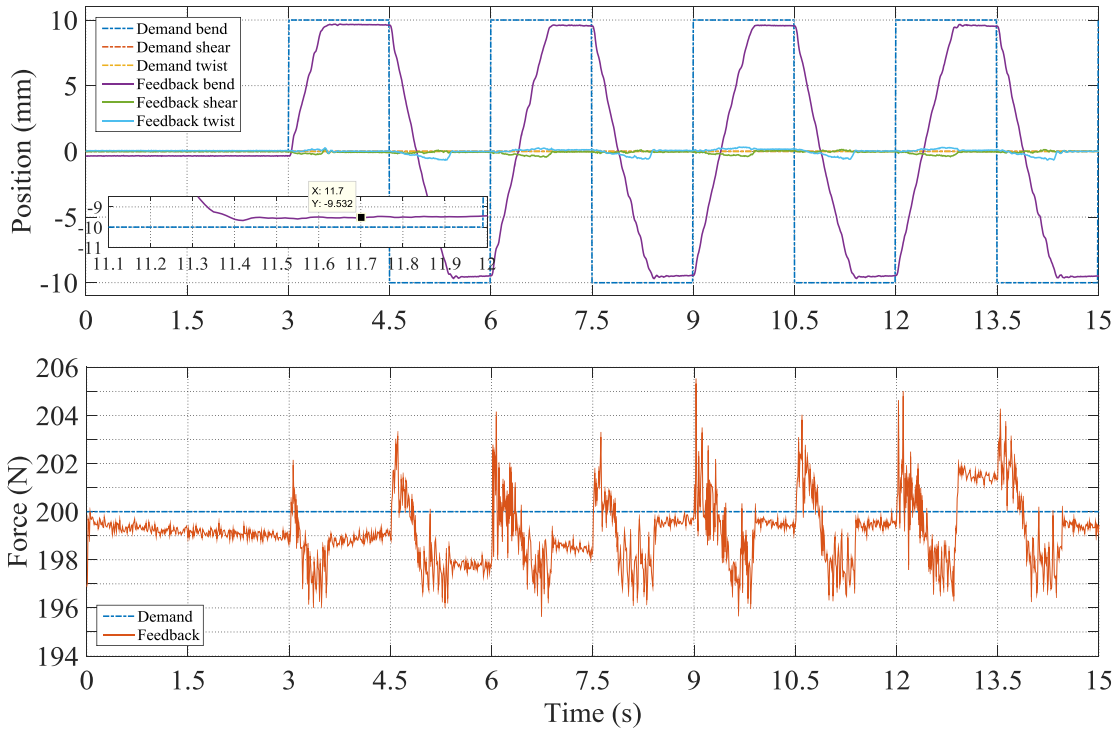

Fig. 16. Experimental responses with square position demand of 10 mm in bend, force demand of 200 N, B = 0.4 mm and B_f = 3 N

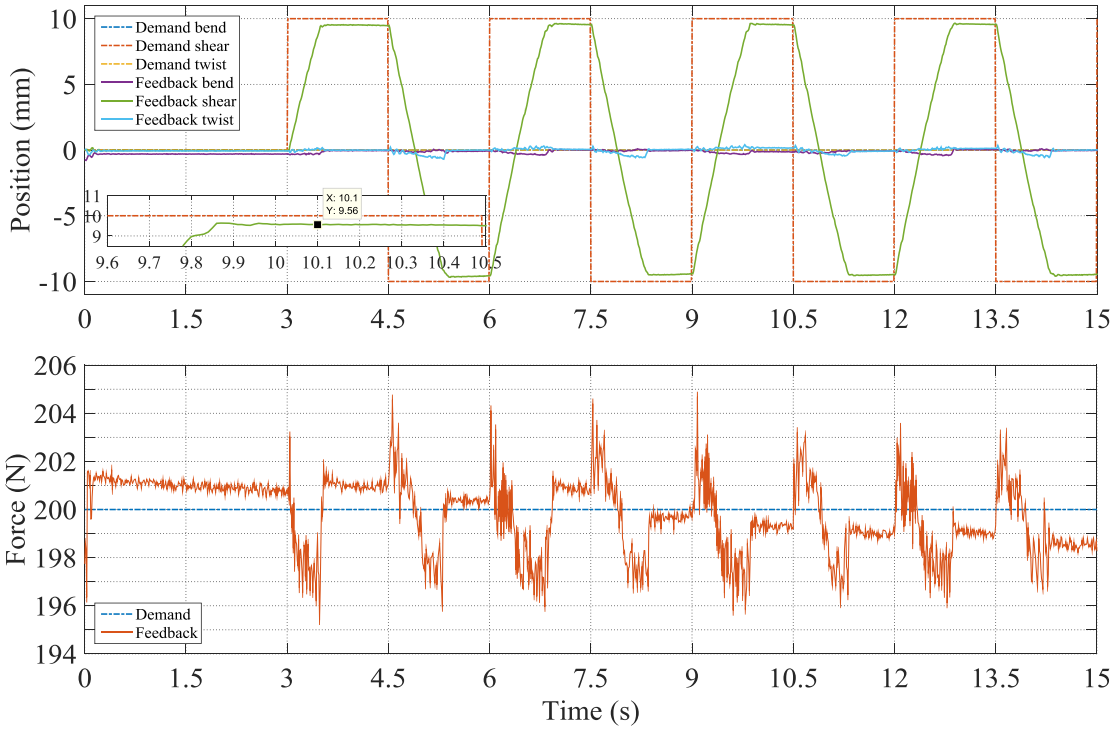

Fig. 17. Experimental responses with square position demand of 10 mm in shear, force demand of 200 N, B = 0.4 mm and B_f = 3 N

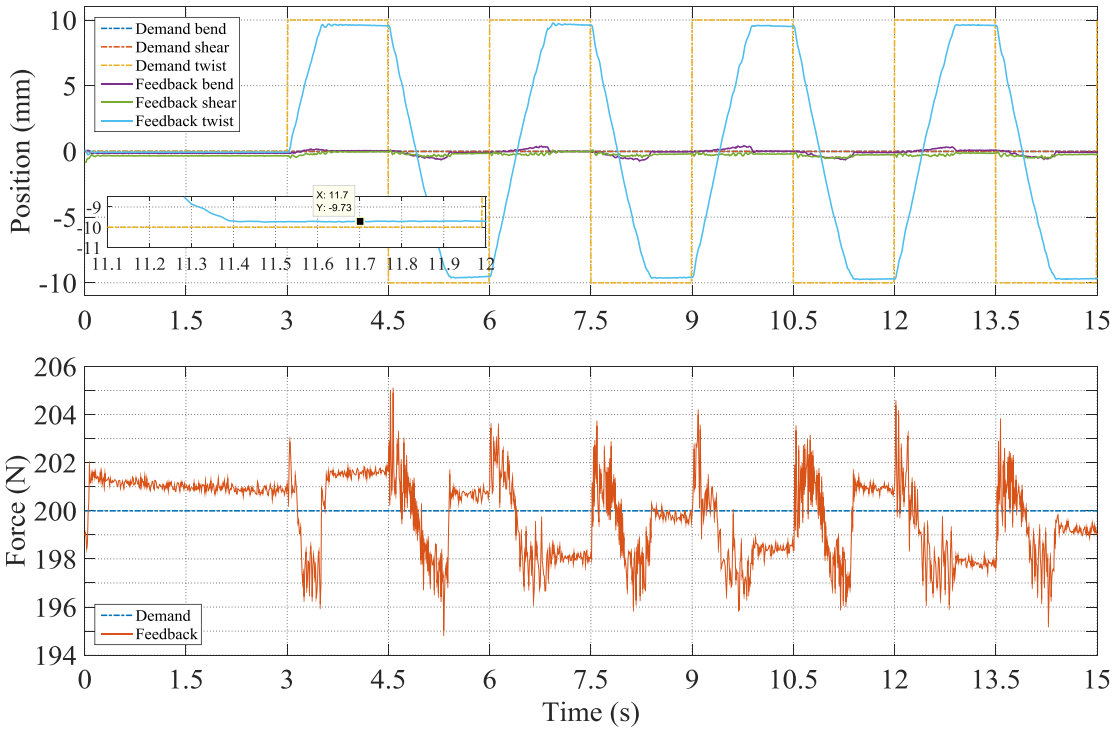

Fig. 18. Experimental responses with square position demand of 10 mm in twist, force demand of 200 N, B = 0.4 mm and B_f = 3 N

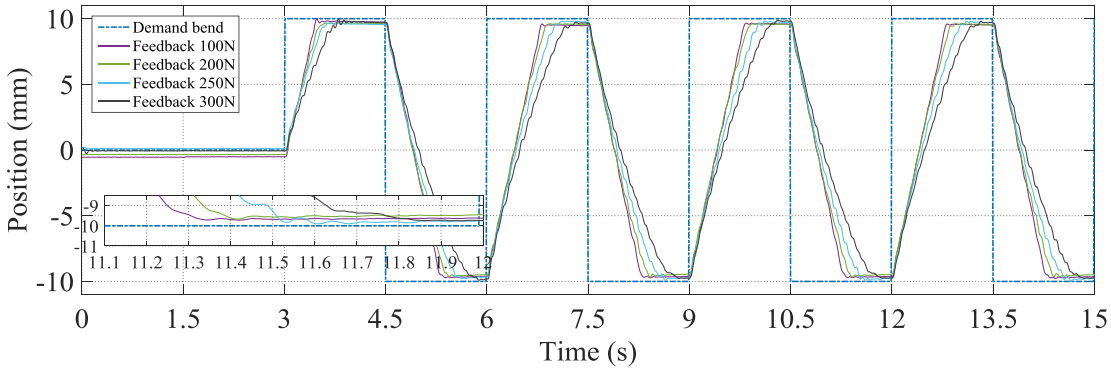

Fig. 19. Experimental responses of various force demands under square position demand of 10 mm in bend, B = 0.4 mm and B_f = 3 N

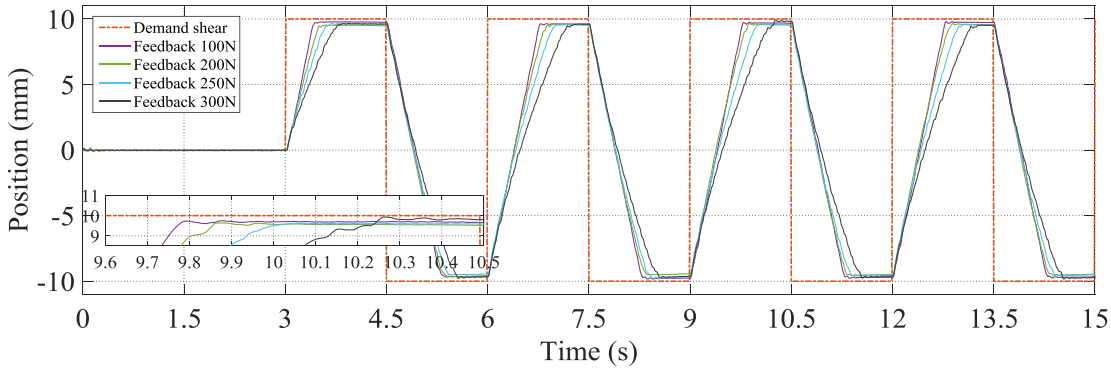

Fig. 20. Experimental responses of various force demands under square position demand of 10 mm in shear, B = 0.4 mm and B_f = 3 N

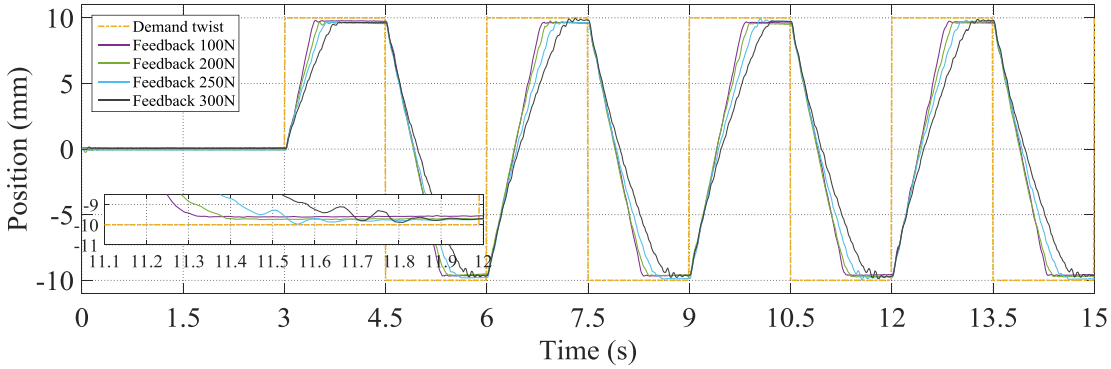

Fig. 21. Experimental responses of various force demands under square position demand of 10 mm in twist, B = 0.4 mm and B_f = 3 N

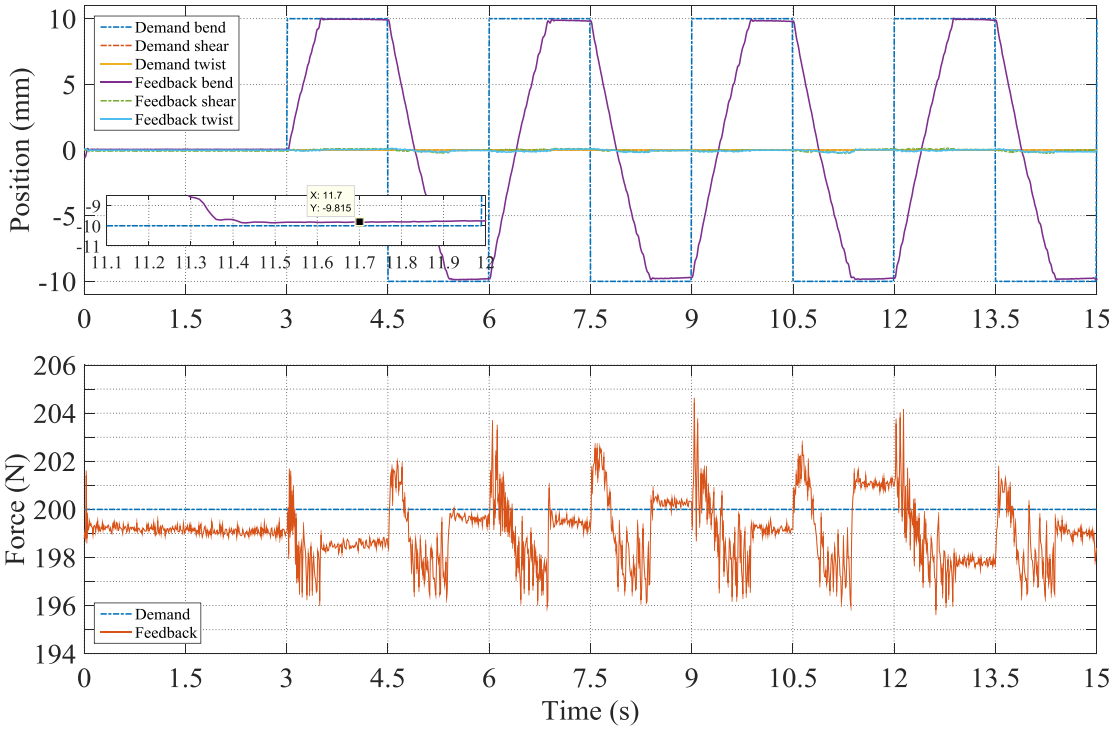

Fig. 22. Experimental responses of one cell with square position demand of 10 mm in bend, force demand of 200 N, B = 0.2 mm and B_f = 3 N

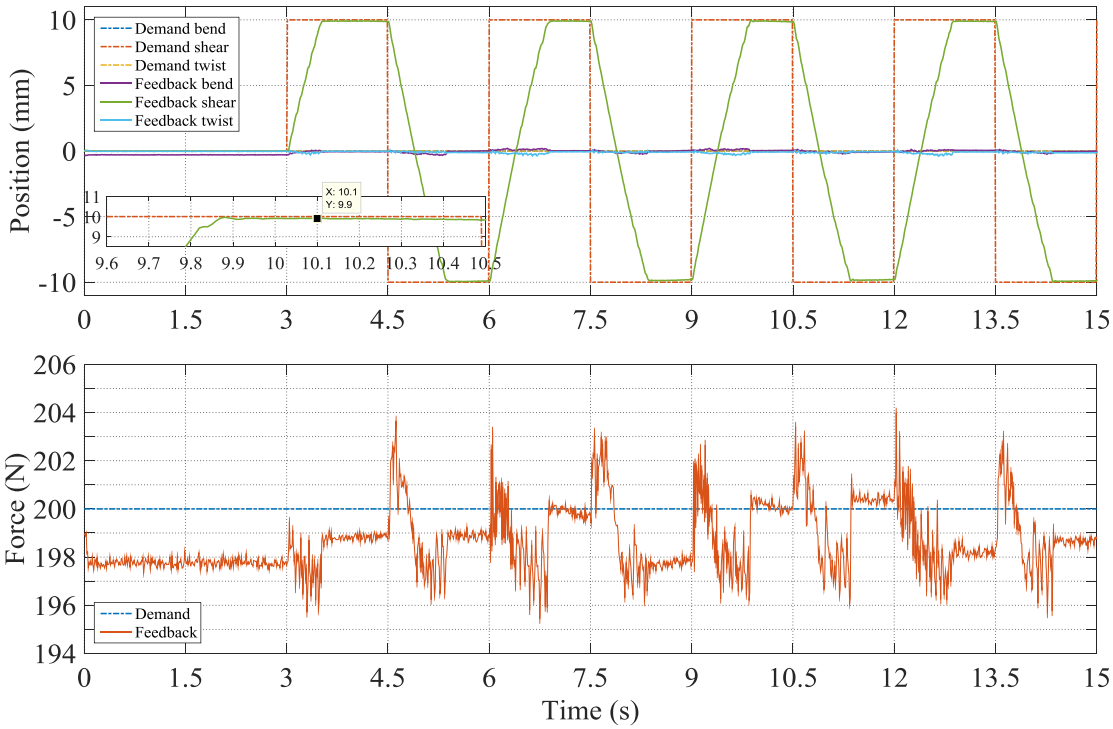

Fig. 23. Experimental responses of one cell with square position demand of 10 mm in shear, force demand of 200 N, B = 0.2 mm and B_f = 3 N

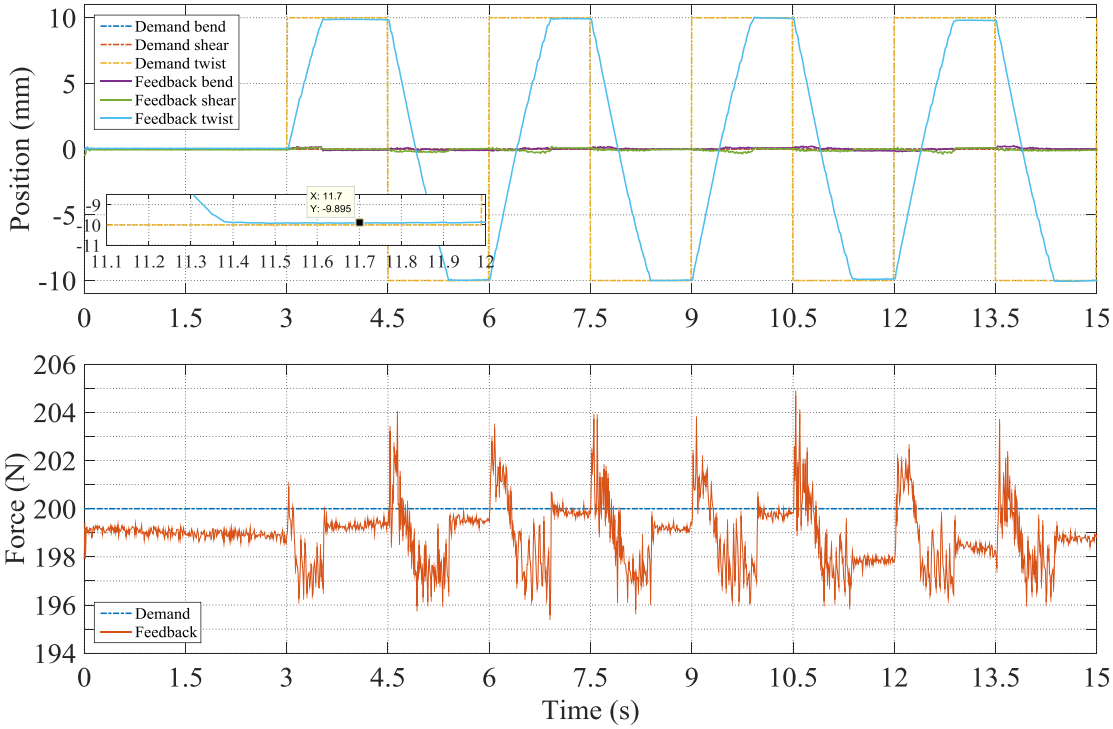

Fig. 24. Experimental responses of one cell with square position demand of 10 mm in twist, force demand of 200 N, B = 0.2 mm and B_f = 3 N

5.2 Small amplitude sine wave position demand

To see the performance with a sinusoidal position demand, a sine wave position demand of 10 mm amplitude and 3 s period is used in turn for each degree of freedom with the force demand fixed at 200 N. The tolerance settings are B = 0.4 mm and B_f = 3 N in all cases. The experimental results are illustrated in Figs. 25 to 27. It can be seen that the experimental system performs well in both position tracking and force keeping. However, a high frequency oscillation (about 30Hz) is evident, particularly in the bend and twist tracking cases. This is an inevitable consequence of the discontinuous controller attempting to track the continually varying demand signal. The frequency of oscillation is linked to the position error dead band setting in the controller (0.2mm in this case), as well as the rate of change of the demand. The oscillation amplitude is quite small in this case, but care would need to be exercised that the switching action did not excite resonant modes of the structure.

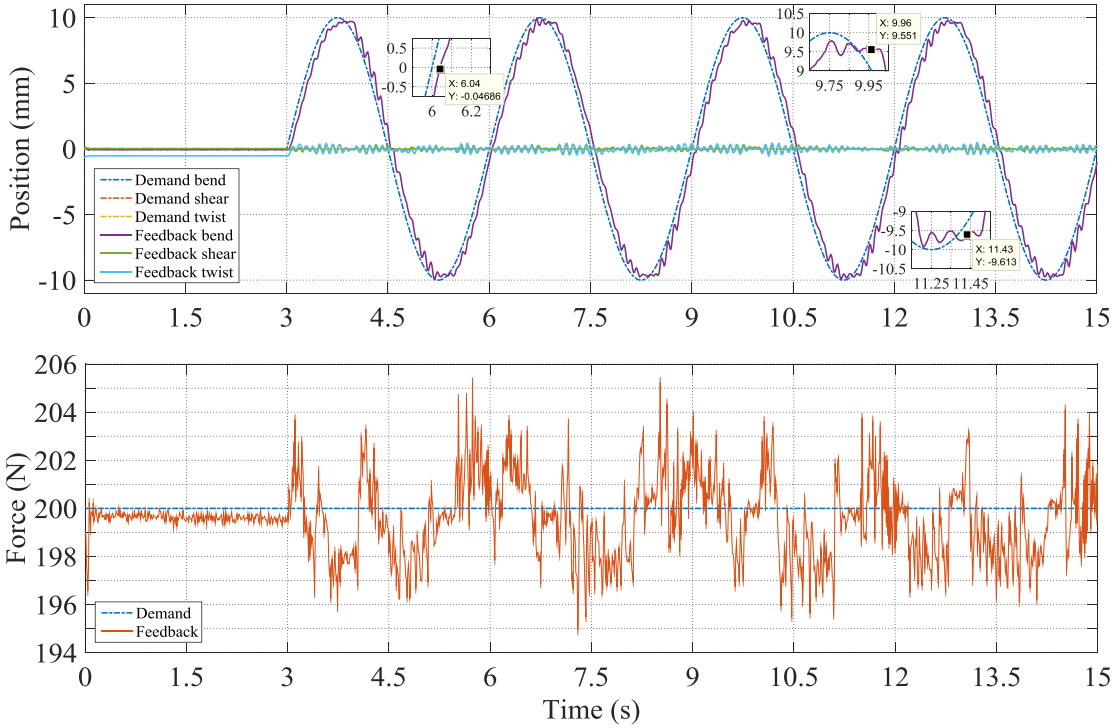

Fig. 25. Performance with sinusoidal position demand of 10 mm in bend and force demand of 200 N

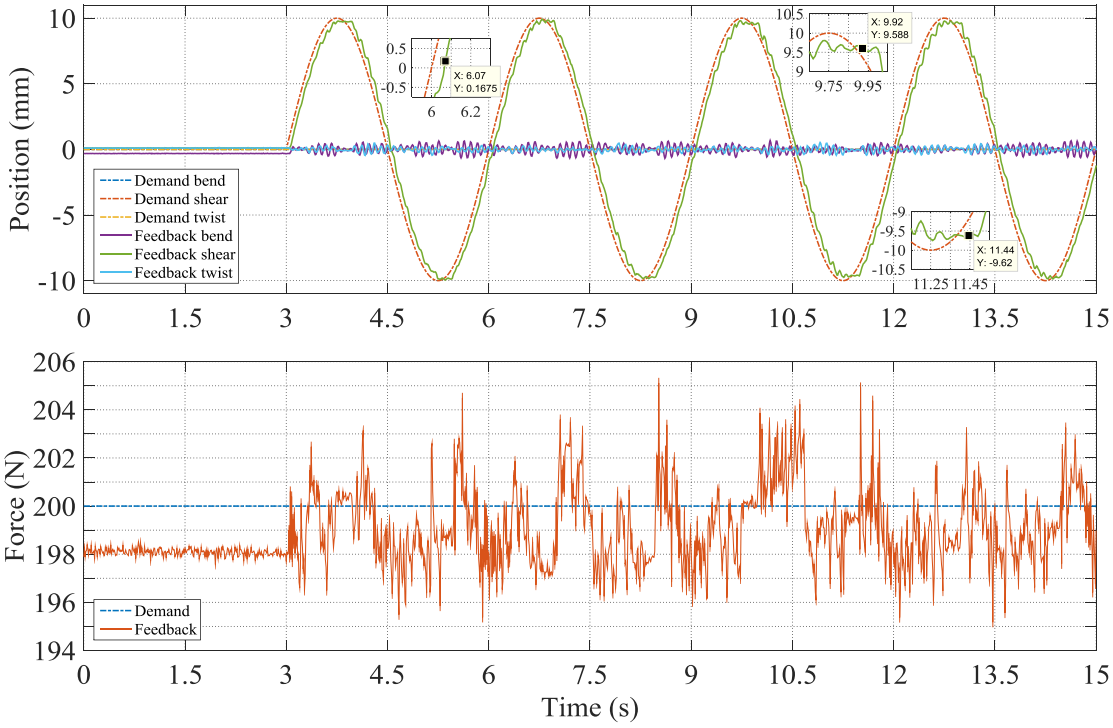

Fig. 26. Performance with sinusoidal position demand of 10 mm in shear and force demand of 200 N

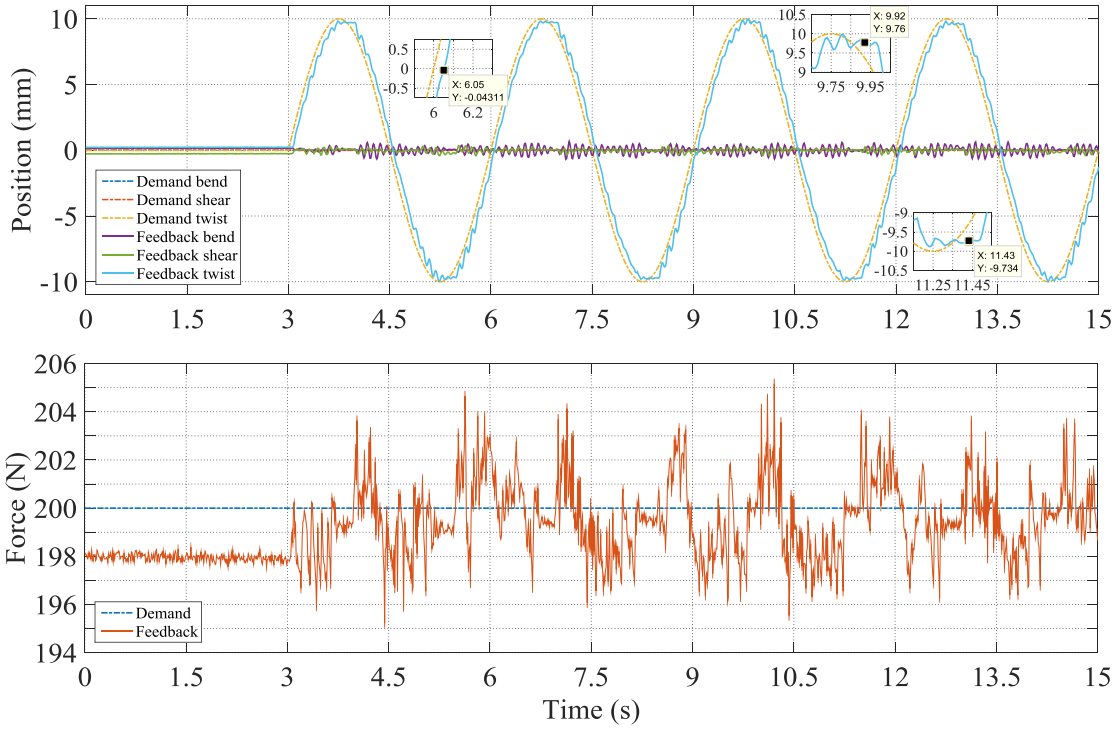

Fig. 27. Performance with sinusoidal position demand of 10 mm in twist and force demand of 200 N

5.3 Large amplitude position demand

The experimental tensegrity system is also tested with a square and a sine wave of 40 mm amplitude. The difference in forces between the PAMs becomes greater at higher displacements. And so to keep the highest actuator force to a reasonable level, the force demand is reduced to 100 N in this series of tests. The position and force tolerances are $B = 0.4$ mm and $B_f = 3$ N. The results of the bending experiments are shown in Figs. 28 and 29. The motions in shear and twist show very similar results. The experimental system responds well to these two position demands with large amplitudes while maintaining the required pre-load.

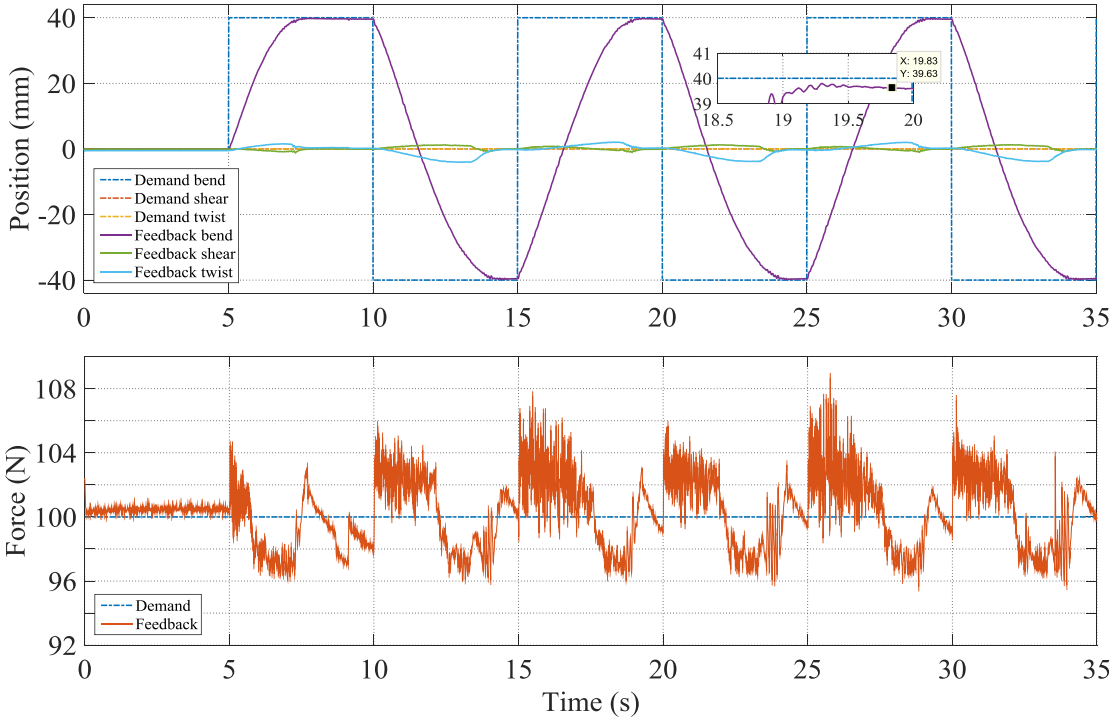

Fig. 28. Experimental responses with square position demand of 40 mm in bend

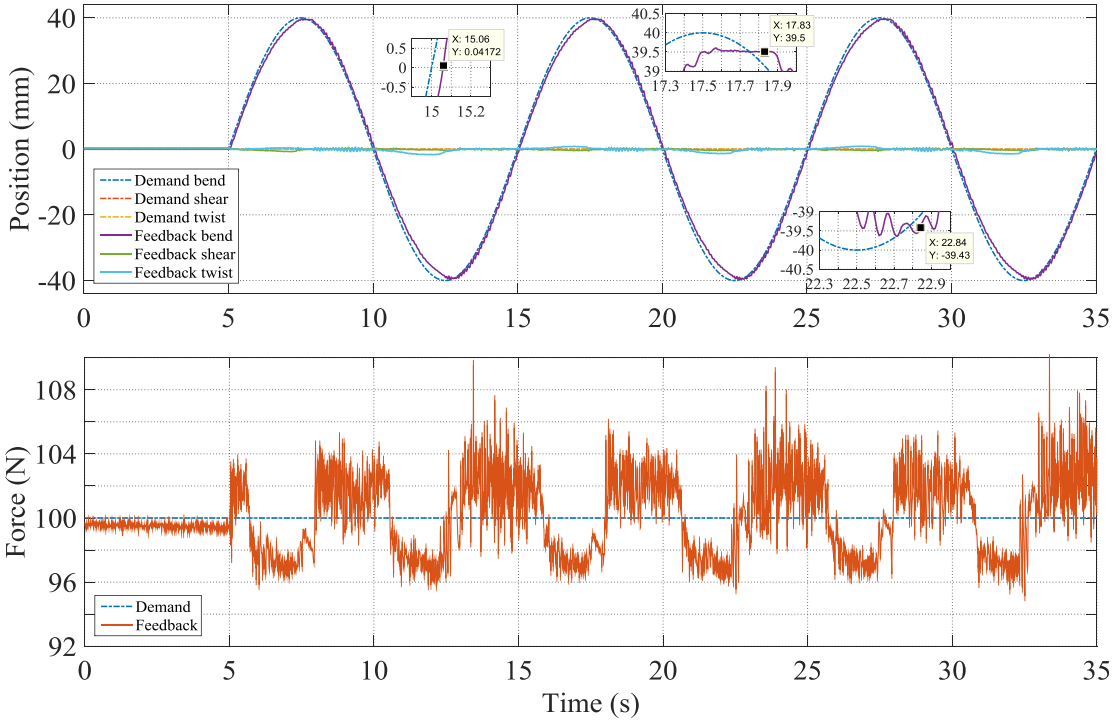

Fig. 29. Performance of tracking sinusoidal position demand of 40 mm in bend

5.4 Experiments with mixed position demand

A final demonstration is given in Figs. 30 and 31 for mixed position demands of 14, 12 and 10 mm in bend, shear and twist, respectively. The force demand is set to 150 N. For the results of square wave

position demand, variations of force, pressure and displacement (from the 290 mm nominal length) in the PAMs are also provided in Fig. 32. The experimental system performs well in these two tests.

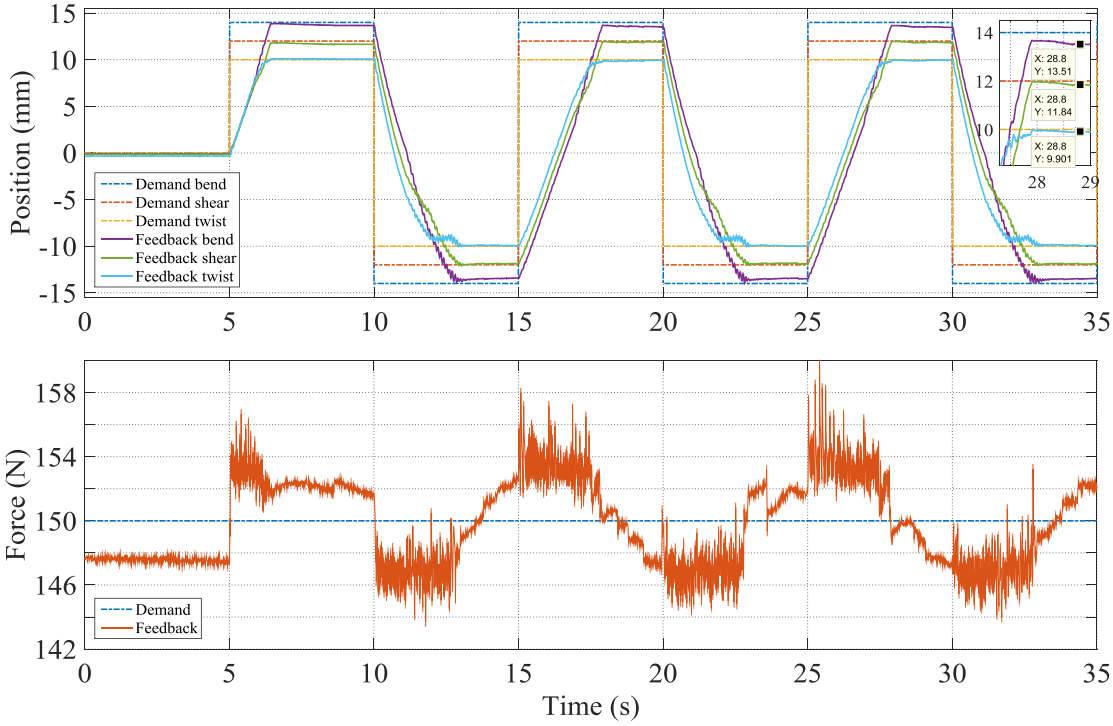

Fig. 30. Performance under mixed square position demand with force demand of 150 N, B = 0.4 mm and B_f = 3 N

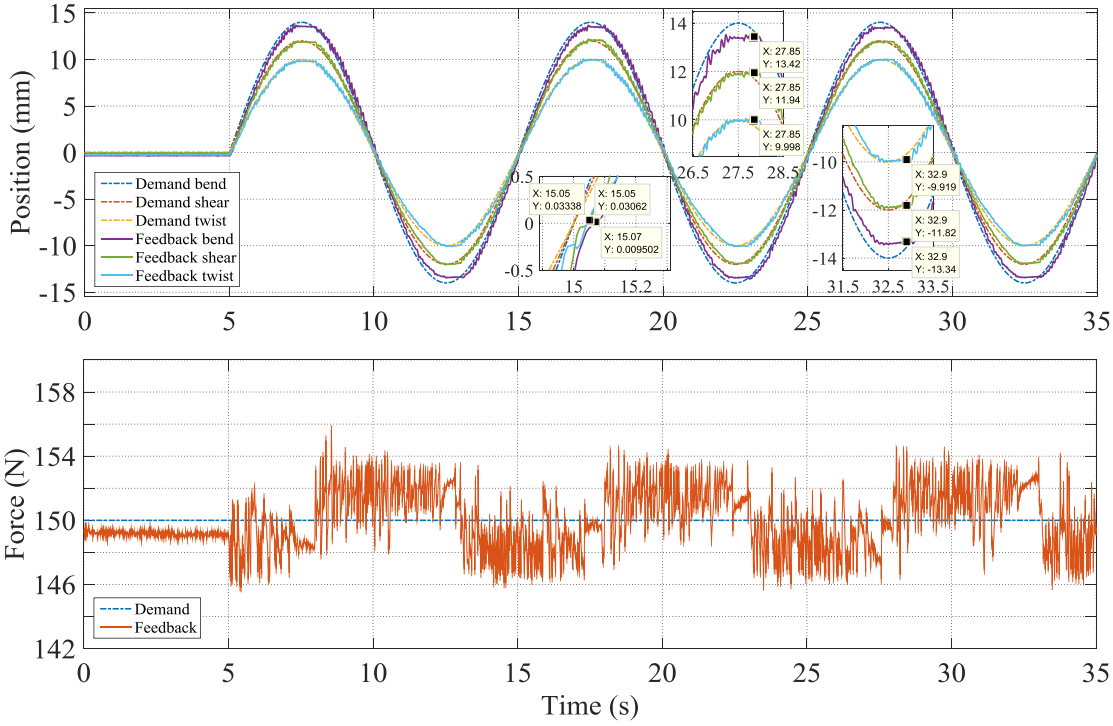

Fig. 31. Performance under mixed sinusoidal position demand with force demand of 150 N, B = 0.4 mm and B_f = 3 N

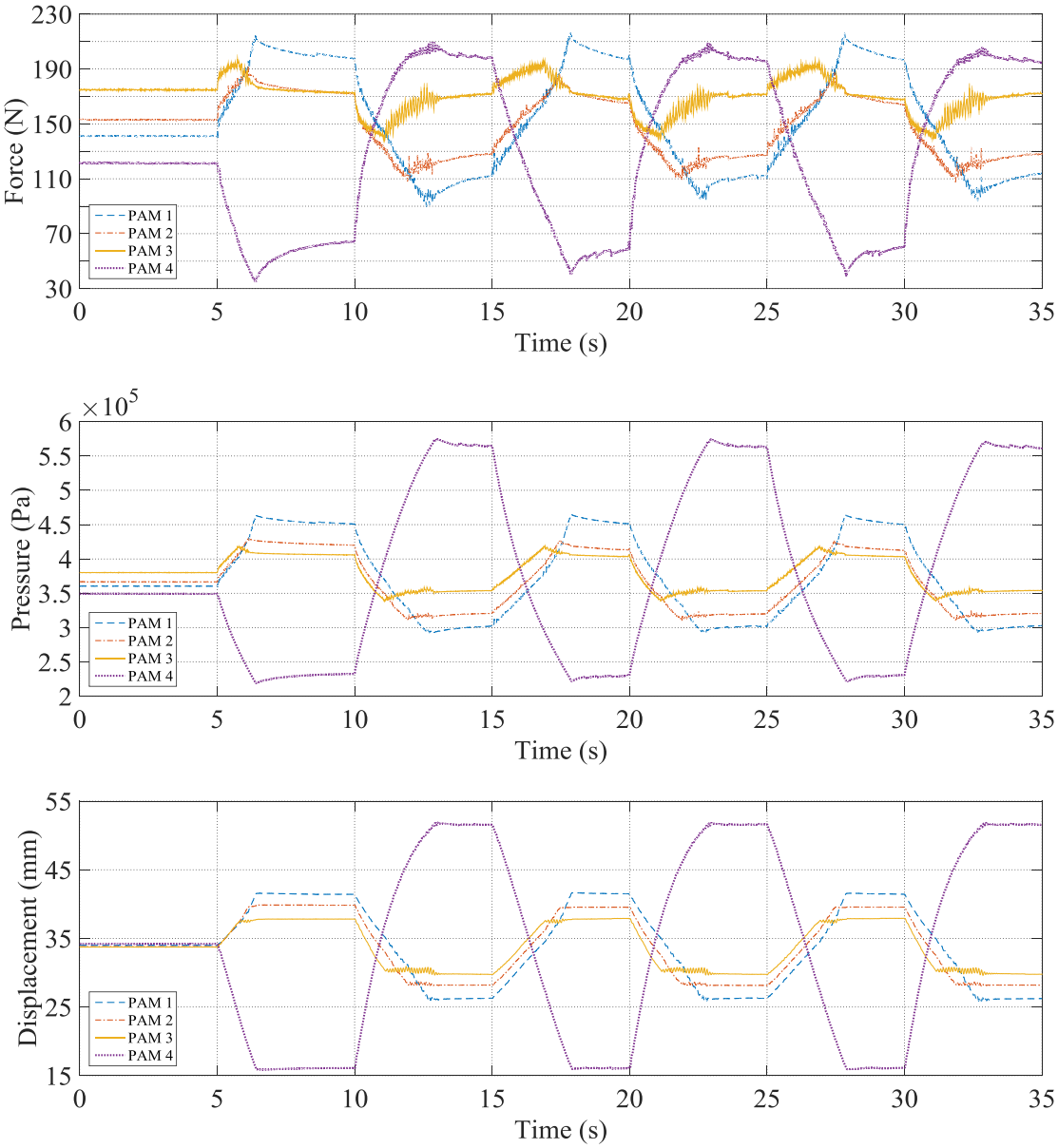

Fig. 32. Force, pressure and displacement variations in the PAMs during the motion with mixed square position demand

6 Conclusions

This paper describes the development and testing of new structures with integrated multi-axis shape changing capability. An actuated tensegrity structure concept is proposed, for which a form-finding method has been derived, allowing stable structural configurations to be found. The method considers the real-life issue that members meeting at a node cannot meet at a single point i.e. nodes with finite dimensions and rotational degrees-of-freedom are included. In a tensegrity structure, some members are only ever in tension, and others are only ever in compression, and no members experience bending moments, leading to a structure with the potential for a high stiffness-to-weight ratio. In our novel

actuated structures, either tensile members or compressive members can be replaced by actuators, although tensile actuators benefit from avoiding buckling issues, and only tensile actuators are demonstrated in this work.

An antagonistic multi-axis closed loop control scheme is presented allowing actuated members to be controlled co-operatively to provide simultaneous shape change in multiple directions, while controlling the pre-load within the structure. Although demonstrated for a four-actuator structure, the method is quite general and can be applied to structures with any number of actuated members. Particularly in complex structures, a rigorous mathematical approach is crucial for transforming between actuator and structural shape co-ordinates to ensure the position and force loops act in a consistent manner. Measurement of individual actuator position and force is required.

An example actuated tensegrity system has been designed and built, containing 9 nodes, 9 compressive members, 10 passive tensile members and 4 actuated tensile members. The actuators used are Pneumatic Artificial Muscles (PAMs). PAMs or other fluid actuators (pneumatic or hydraulic) are particularly well suited to this application due to their low weight for specific power or force requirements, thus keeping the structure lightweight. Each PAM length is measured by a wire-pull potentiometer, and PAM force is estimated from the internal air pressure. Air flow into and out of each PAM is controlled by a pair of high speed on-off valves. The relay-type control that this necessitates has led to the development and analysis of a dead-band controller. The describing function technique has been used to analyse the stability of this controller, and a stability criterion has been derived. The criterion indicates that increasing the damping coefficient, increasing the size of the dead band, or reducing the mass will tend to stabilize the system.

The experimental system has successfully demonstrated the overall concept of using a tensegrity structure to develop a load-bearing structure with shape-changing capability. The control performance of the experimental actuated tensegrity system is good. The antagonistic control of the four tensile members within the geometrical configuration of the example tensegrity structure achieves accurate control of three independent motions (bend, shear and twist) along with the control of the internal structure pre-load. This controller has been developed with the help of a validated simulation model of the system, which is reported elsewhere [44].

Through analysis and experimentation, this paper has shown the potential for creating morphing structures with integrated actuation under closed loop control, with potential application to a wide variety of future dynamic lightweight machines. A motivation for this work is the development morphing aerospace structures. Compared to other approaches, it is relatively easy to integrate a variety of actuator technologies (conventional or experimental) to create an active tensegrity structure,

meanwhile maintaining a structurally efficient design in terms of achieving required stiffness and strength with low mass. In our on-going research we are using the approach to create a morphing wing for wind-tunnel testing. In addition, we are developing detailed dynamic models to facilitate optimisation of dynamic properties and to support controller design, and which will complement the simplified modelling contained in this paper.

Acknowledgement

The authors wish to thank Moog Aircraft Group and the University of Bath for providing financial support for this research.

References

[1] S. Barbarino, O. Bilgen, R. M. Ajaj, M. I. Friswell, and D. J. Inman, "A Review of Morphing Aircraft," Journal of Intelligent Material Systems and Structures, vol. 22, pp. 823-877, Jun 2011.

[2] K. Miura, "Design and operation of a deployable truss structure," in 18th Aerospace Mechanisms Symposium, Goddard Space Flight Center, Greenbelt, Maryland, 1984.

[3] K. Miura, H. Furuya, and K. Suzuki, "Variable geometry truss and its application to deployable truss and space crane arm," Acta Astronautica, vol. 12, pp. 599-607, 1985.

[4] D. S. Ramrakhyani, G. A. Lesieutre, M. I. Frecker, and S. Bharti, "Aircraft Structural Morphing using Tendon-Actuated Compliant Cellular Trusses," Journal of Aircraft, vol. 42, pp. 1614-1620, 2005/11/01 2005.

[5] A. Y. N. Sofla, D. M. Elzey, and H. N. G. Wadley, "Shape morphing hinged truss structures," Smart Mater. Struct., vol. 18, 2009.

[6] A. Y. N. Sofla, D. M. Elzey, and H. N. G. Wadley, "A rotational joint for shape morphing space truss structures," Smart Materials and Structures, vol. 16, pp. 1277-1284, Aug 2007.

[7] A. Moosavian, F. F. Xi, and S. M. Hashemi, "Design and Motion Control of Fully Variable Morphing Wings," Journal of Aircraft, vol. 50, pp. 1189-1201, Jul-Aug 2013.

[8] C. Sultan, “Tensegrity: sixty years of art, science, and engineering,” Adv.Appl.Mech.43,69–145. 2009.

[9] R. B. Fuller, "Tensile-Integrity Structures," U.S. Patent 3 063 521, 1962.

[10] D. G. Emmerich, “Emmerich on self-tensioning structures,” International Journal of Space Structures, 11(1–2), 29–36. 1996

[11] J. Y. Zhang, S. D. Guest, and M. Ohsaki, "Symmetric prismatic tensegrity structures. Part II: Symmetry-adapted formulations," International Journal of Solids and Structures, vol. 46, pp. 15-30, Jan 2009.

[12] J. Y. Zhang, S. D. Guest, R. Connelly, and M. Ohsaki, "Dihedral 'star' tensegrity structures," International Journal of Solids and Structures, vol. 47, pp. 1-9, Jan 2010.

[13] K. Koohestani and S. D. Guest, "A new approach to the analytical and numerical form-finding of tensegrity structures," International Journal of Solids and Structures, vol. 50, pp. 2995-3007, Sep 2013.

[14] K. Koohestani, "A computational framework for the form-finding and design of tensegrity structures," Mechanics Research Communications, vol. 54, pp. 41-49, Dec 2013.

[15] H. C. Tran and J. Lee, "Form-finding of tensegrity structures using double singular value decomposition," Engineering with Computers, vol. 29, pp. 71-86, Jan 2013.

[16] L. Y. Zhang, Y. Li, Y. P. Cao, and X. Q. Feng, "Stiffness matrix based form-finding method of tensegrity structures," Engineering Structures, vol. 58, pp. 36-48, Jan 2014.

[17] G. Tibert, & S. Pellegrino, S. "Review of form-finding methods for tensegrity structures." International Journal of Space Structures, 18(4), 209–223, 2003

[18] R. E. Skelton and M. C. Oliveira, Tensegrity Systems, 1. ed. Boston, MA: Springer US, 2009.

[19] A. Plummer and G. Lai, "New concepts for parallel kinematic mechanisms using fluid actuation," presented at the 7th International conference on Fluid Power and Mechatronics, Harbin, 2015.

[20] S. Djouadi, R. Motro, J.C. Pons, & B. Crosnier, "Active control of tensegrity systems," ASCE Journal of Aerospace Engineering, 11(2), 37–44. 1998

[21] J. B. Aldrich, R. E. Skelton, K. Kreutz-Delgado, Aac, and Aac, "Control synthesis for a class of light and agile robotic tensegrity structures," in Proceedings of the 2003 American Control Conference, Vols 1-6, ed New York: Ieee, 2003, pp. 5245-5251.

[22] C. Sultan, M. Corless, R.E.Skelton, "Tensegrity flight simulator." Journal of Guidance, Control, and Dynamics, 23, 1055–1064, 2000

[23] N. Bel Hadj Ali, I.F.C., Smith, "Dynamic behavior and vibration control of a tensegrity structure", International Journal of Solids and Structures, Volume 47, Issue 9, Pages 1285-1296, 2010

[24] H. Beck, J. Cooper, C., "Kurilpa Bridge" Images Publishing Group, 2012.

[25] H. Benaroya, "Tensile-Integrity Structures for the Moon," Applied Mechanics Reviews, vol. 46, p. 326, 1993.

[26] A. G. Tibert and S. Pellegrino, "Deployable tensegrity reflectors for small satellites," Journal of Spacecraft and Rockets, vol. 39, pp. 701-709, Sep-Oct 2002.

[27] K. Caluwaerts, J. Despraz, A. Iscen, A. P. Sabelhaus, J. Bruce, B. Schrauwen, et al., "Design and control of compliant tensegrity robots through simulation and hardware validation," Journal of the Royal Society Interface, vol. 11, p. 13, Sep 2014.

[28] Y. C. Toklu, R. Temur, G. Bekdas, and F. Uzun, "Space Applications of Tensegric Structures," in Proceedings of 6th International Conference on Recent Advances in Space Technologies, Istanbul, 2013, pp. 29-32.

[29] K. W. Moored and H. Bart-Smith, "The analysis of tensegrity structures for the design of a morphing wing," Journal of Applied Mechanics-Transactions of the Asme, vol. 74, pp. 668-676, Jul 2007.

[30] K. W. Moored and H. Bart-Smith, "Investigation of clustered actuation in tensegrity structures," International Journal of Solids and Structures, vol. 46, pp. 3272-3281, 8/15/ 2009.

[31] K. Salisbury, W. Townsend, B. Ebrman, and D. DiPietro, "Preliminary design of a whole-arm manipulation system (WAMS)," in Robotics and Automation, 1988. Proceedings., 1988 IEEE International Conference on, 1988, pp. 254-260 vol.1.

[32] A. Bicchi and G. Tonietti, "Fast and "soft-arm" tactics," IEEE Robotics & Automation Magazine, vol. 11, pp. 22-33, Jun 2004.

[33] J. He, R. Liu, K. Wang, and H. Shen, "The mechanical design of snake-arm robot," in IEEE 10th International Conference on Industrial Informatics, Beijing, China, 2012, pp. 758-761.

[34] R. Buckingham and A. Graham, "Snaking around in a nuclear jungle," Industrial Robot-An International Journal, vol. 32, pp. 120-127, 2005.

[35] R. Bloss, "Robotic snake arm reaches into radioactive regions," Industrial Robot-An International Journal, vol. 38, pp. 200-201, 2011.

[36] C. Sultan, "Stiffness formulations and necessary and sufficient conditions for exponential stability of prestressable structures." International Journal of Solids and Structures 50.14-15 2180-2195. 2013

[37] J.J. Craig, "Introduction to Robotics: Mechanics and Control." Pearson, 4th Ed. 2018.

[38] S. Guest, "The stiffness of prestressed frameworks: A unifying approach," Int. J. Solids Struct., vol. 43, pp. 842-854, 2006.

[39] G. Lai, A. R. Plummer, D. J. Cleaver, and H. Zhou, "Parallel kinematic mechanisms for distributed actuation of future structures," Journal of Physics: Conference Series, vol. 744, p. 012169, 2016.

[40] G. Lai, "Distributed Actuation and Control for Morphing Structures," Thesis (Ph.D.) - University of Bath, Bath, 2017.

[41] A. Plummer, "A general co-ordinate transformation framework for multi-axis motion control with applications in the testing industry," Control Engineering Practice, vol. 18, pp. 598-607, Jun 2010.

[42] G. Lai and A. Plummer, "Relay Control of a Morphing Tensegrity Structure with Distributed Pneumatic Actuation," presented at the The 9th International Conference on Fluid Power Transmission and Control, Zhejiang University, 2017.

[43] T. Dougherty, Systems & Control: An Introduction to Linear, Sampled & Non-linear Systems. Singapore: World Scientific, 1995.

[44] G. Lai, A. Plummer, and D. Cleaver, "The development and validation of a dynamic model for a tensegrity structure with distributed actuation," Proceedings of the Institution of Mechanical Engineers, Part I: Journal of Systems and Control Engineering. Under review.

[45] B. Tondu, "Modelling of the McKibben artificial muscle: A review," Journal of Intelligent Material Systems and Structures, vol. 23, pp. 225-253, Feb 2012.

Guanyu Lai received his Ph.D degree from the University of Bath in 2017, for research in the field of distributed actuation and control of active structures. His main research interests include motion and force control of multi-axis systems, modelling and simulation of dynamic systems, and active structures. He was given the Best Paper award of the Global Fluid Power Society in the 9th International Conference on Fluid Power Transmission and Control (ICFP2017), Zhejiang University, Hangzhou, China.

Andrew Plummer received his Ph.D degree from the University of Bath in 1991, for research in the field of adaptive control of electro-hydraulic systems. He worked as a research engineer for Rediffusion Simulation (now Thales Training and Simulation) from 1990, developing motion and control loading system technology, before taking up a lecturing post in Control Systems and Mechatronics at the University of Leeds in 1994. From 1999 until 2006 he was global control systems R&D manager for Instron, manufacturers of materials and structural testing systems. He is Director of the Centre for Power Transmission and Motion Control. He has a variety of research interests in the field of motion and force control, including inverse-model based control of electro-hydraulic servo-systems, control of parallel kinematic mechanisms, hybrid hydraulic/piezoelectric actuation, and robot control. Prof. Plummer is Past Chair of the Institution of Mechanical Engineers Mechatronics Informatics and Control Group and also the UK Automatic Control Council, and is Associate Editor of both the International Journal of Fluid Power and Control Engineering Practice. He chairs the Global Fluid Power Society.

David James Cleaver is a Lecturer in Aerospace Engineering within the Department of Mechanical Engineering at University of Bath. His research expertise includes unsteady aerodynamics for micro air vehicles, vortical flows, experimental methods, aeroelasticity and Unmanned Aircraft Systems. David has led and participated on projects funded by the US Air Force Office of Scientific Research, US Office of Naval Research Global, UK Engineering and Physical Sciences Research Council, UK Department for Transport and Innovate UK. These projects involved collaboration with the US Air Force Research Laboratory, Airbus UK, SalusUAV and Siemens UK. Outcomes from this work include new understanding of fundamental flow phenomenon like lift enhancement due to convected vortices and deflected jets, thrust enhancement due to vortical fluid structure interactions, reduced order modelling for wing load estimation and new approaches to unmanned flight. These outcomes have been disseminated through publication in internationally renowned journals such as Progress in Aerospace Sciences, the Journal of Fluid Mechanics, and the AIAA Journal, and regular presentations at AIAA conferences.